

# Aluminum Nano-composites for Elevated Temperature Applications

by

Cecilia Borgonovo

A Thesis

Submitted to the Faculty

of the

WORCESTER POLYTECHNIC INSTITUTE

*in partial fulfillment of the requirements for the*

Degree of Master of Science

in

Material Science & Engineering

June 2010

APPROVED:

*Diran Apelian*, Advisor  
Howmet Professor  
Director of Metal Processing Institute



*Richard D. Sisson Jr.*  
George F. Fuller Professor  
Director of Manufacturing and Materials Engineering



## *Abstract*

Conventional manufacturing methods are sub-optimal for nano-composites fabrication. Inhomogeneous dispersion of the secondary phase and scalability issues are the main issues. This work focuses on an innovative method where the reinforcement is formed *in-situ* in the melt. It involves the reaction of the molten aluminum with a nitrogen-bearing gas injected through the melt at around 1273 K. AlN particles are expected to form through this in situ reaction. A model has been developed to predict the amount of reinforced phase. Experiments have been carried out to confirm the feasibility of the process and the mechanism of AlN formation discussed. The detrimental effect of oxygen in the melt which hinders the nitridation reaction has been proved. The effect of process times and the addition of alloying elements (Mg and Si) have also been investigated.

## *Acknowledgments*

First of all, I really would like to thank my advisor, Professor Diran Apelian. He taught me how to approach scientific research. He provided me with a different look of the world and guided me through the issues that I encountered during my investigation. He is my model not only as an engineer, but as a fulfilled and illuminated person. He supported me in several times and never left me alone.

I want to thank Professor Makhoul M. Makhoul for the incredible help in my experiments and for the additional value that his experience has provided to my work. His continuous drive towards new ideas has inspired my research.

I also would like to thank all my colleagues and friends: Lance Wu, Shimin Li, Ning Sun, Hao Yu, Muhammad Qaiser Saleem, Kimon Symeonidis. Thanks also to Professor Libo Wang for his support in my experiments and characterization. I want to express my gratitude to Carol Garofoli, which I also consider a good friend and to Maureen Plunkett. Thanks to Carl Raatikainen for his help with the experimental apparatus.

Last but not less important, I thank my family that always supported me even from the other side of the ocean and that never stopped believing in me. I dedicate my thesis to my grandfather who passed me the love for engineering and his creativity.

# Table of Contents

<i>Abstract</i> .....	ii
<i>Acknowledgements</i> .....	iii
<i>Table of Contents</i> .....	iv
Executive Summary.....	1
1. Motivations behind current work	
1.1 High-performances and fuel efficiency: unsuitability of cast alloys	
1.2 Nanocomposite materials as an excellent solution	
2. Objectives	
3. Methodology	
4. Outcomes	
<i>References</i>	
Appendices	
<b>Appendix A:</b> "Manufacture of Aluminum Nanocomposites: <i>A Critical Review</i> ".....	6
<b>Appendix B:</b> "In-situ Processing of Aluminum Based Nanocomposites: <i>Model and Experimental Validation</i> ".....	42
Recommendations for Future Work.....	80

# Executive Summary

## 1. Motivation

### *1.1 High-performances and fuel efficiency: unsuitability of cast alloys*

Globalization stimulates innovation in technologies, products and processes. Today's main challenge is to satisfying the requests of a continuously changing world market and at the same time improving performances. For what concerns the automotive markets, three are the factors that dictate the need of a massive substitution of aluminum for steel.

- *Gas price:* it has reached 9 USD per gallon in Europe (July 2008) [1]. Gas consumption is bonded to vehicle weight. The use of aluminum would be advantageous for the overall vehicle weight, since its density is one third of steel ( $2.7 \text{ g/cm}^3$ ).
- *CO<sub>2</sub> Emission limits:* according to EU-Regulation it will be 120 g/km by 2012 [1]. Weight saving materials lead to a better fuel efficiency and therefore, lower emissions.
- *Recycling:* recycling aluminum is tremendously less expensive than producing it. It requires a fraction of the energy and the quality is the same.

The reduction in vehicle weight meets both fuel efficiency and recycling standards. For this reason both aluminum and automotive industries have attempted to make aluminum a cost-effective alternative to steel [2]. Consequently, recent developments regarding automotive materials are oriented to maximize not just the material resistance, though the power to weight ratio ( $R/\rho$ ). In this scenario, Diesel engines have gained a consistent market share not only in Europe but also in the US. The market share of Diesel Engines in Europe is near 50% [3]. The reasons are several:

- Fuel economy (20% less fuel consumption compared to the gasoline engines);
- New technologies (Common Rails, High pressure Direct Injection engines, lean-burn engines) [4];
- Contemporary achievement of SOOT and NO<sub>x</sub> reduction for vehicles built according to EURO 8 regulations (EGR systems, after-treatment systems such as SCR de-NO<sub>x</sub> catalytic systems and anti-particulate filters) [4];
- Improvement of vehicle performance with lower displacement engines [3];
- Tax incentives in European markets [3].

The penetration in US market is mainly related to towing and hauling applications and to the growing of light trucks and SUVs, which is expected to encounter further developments in the next

few years [3]. The heavy growth of new mass markets, like China and India, is also contributing to the massive use of Diesel engines. Therefore, the research is focusing on the improvement of the weight-to-power ratio of this type of engines. As a light material, the use of aluminum for Diesel components is desirable. Despite this, two factors limit the use of aluminum in Diesel applications:

- Current cost of primary aluminum (1.15 \$/lb.) [5];
- The limits of aluminum mechanical properties at high temperatures. With a view to high efficiency, the new Diesel engines are subjected to higher and higher temperatures, with a marked thermal fatigue and creep.

Current aluminum cast alloys cannot cope with temperature around 2000°C and pressures around 200 MPa in the piston crown area. High creep resistance of die-cast aluminum alloys under long-term loading is hardly achieved at temperature exceeding 250 C° [6]. Consequently, the high demand regarding dimensional stability, strength and durability is hard to meet using classical materials and technologies.

### *1.2 Nanocomposite materials as enabling technology*

Nano-structured composites guarantee high strength, wear resistance, hardness and exceptional microstructure stability at high temperatures [7]. They are suitable for high-performance applications where cast alloys or precipitation strengthened material cannot be employed due to their limited properties. Moreover, nanocomposite materials ensure performances far superior than alloys strengthened by micro-size particles. The tensile strength of a 1 % vol.  $Si_3N_4$  reinforced nanocomposite -10 nm- has been found to be comparable to that of a 15 % volume SiC reinforced microcomposites -3.5  $\mu\text{m}$ -. Ren and Chan [8] fabricated 7075 aluminum matrix reinforced with SiC nanoparticles -50 nm- via powder metallurgy, and noticed a particular increased in wear resistance and high temperature creep resistance compared to the composite reinforced by 13  $\mu\text{m}$  SiC particles. Despite the improved properties, some issues in nanocomposite fabrication have been detected. Agglomeration of the reinforcement has often been observed –see Appendix A- together with particle debonding. Conventional fabrication methods have not been able to provide a homogeneous reinforcement distribution nor have they been cost effective, nor have they been industrially scalable. So the challenges are significant but certainly not insurmountable, and thus the *raison d’être* for this work.

## 2. Objectives

The objectives of this project are:

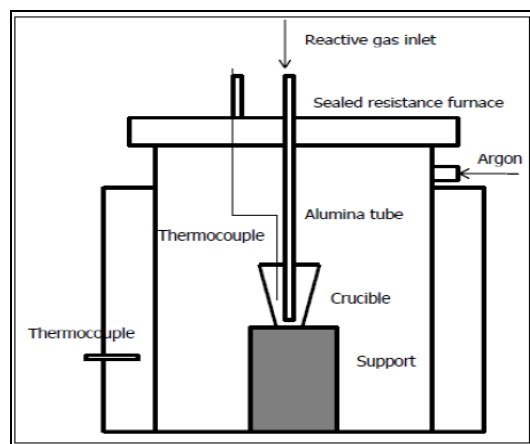
- a. Carry out a critical literature review and determine processing routes worth investigating

- b. Study the feasibility of gas-liquid in-situ method for the production of aluminum matrix nano-composites for high temperature applications.
- c. Study manufacturing issues as well as volume fraction of nano-phase that can be manufactured
- d. Evaluate process scalability.

### 3. Methodology

The following approach has been adopted:

- An extensive *literature review* concerning methods to manufacture aluminum nanocomposites has been carried out –see Appendix A-. Each process has been described and its issues underlined. Ex-situ techniques where the reinforcement is added externally are illustrated as well as in-situ techniques where the reinforcement is synthesized in the matrix by an exothermic reaction.



**Schematic of in situ gas assisted process**

- The most promising manufacturing method has been sorted out and selected as objective of the investigation. An *in-situ gas assisted fabrication technique* –see Appendix A- has been chosen. The process involves the injection of a nitrogen-bearing gas in the reactive melt where liquid nitridation reaction occurs and AlN particles are synthesized – see above. Clean and thermodynamically stable interfaces, lack of detrimental phases and negligible process costs are attractive features of the in-situ method.
- *Edisonian approach*: a set of experiments was pursued to determine the feasibility of the process. The complexity of the set-up and the numerous variables involved –gas flow rate, injection time, temperature, metal surface energy- made such approach sub-optimal and non-suitable to the feasibility study.

- *Modeling feasibility*: a simulation model in COMSOL Multiphysics has been formulated in order to determine the conditions to feasibility. Specifically, the rise of the gas bubble in the melt and the diffusion ahead of the bubble interface has been modeled –see Appendix B-.
- *Experimental verification*: the reliability of the model has been experimentally validated with a series of experiments guided by the model formulation. The impact of oxygen in the melt has been investigated. Different nitrogen-bearing gases (nitrogen and ammonia) and different have been tested and process temperatures in the range of 1273-1323 K adopted. The effect on process feasibility of alloying elements such as Mg and Si has been studied. The goal is to clarify the mechanism of AlN formation, whether it requires the presence of a catalyst –*indirect nitridation*- or not –*direct nitridation*-.

#### 4. Outcomes

The gas-assisted nitridation process has been found to be feasible. The model reliability has been proved. Despite this, the model doesn't account for the addition of catalysts and the detrimental effect of oxygen. Indeed, its detrimental effect of on AlN formation has been confirmed and the need to lead the experiments in an evacuated and inert –Argon-atmosphere underlined. The role of Mg as a catalysis for the reaction has been highlighted. It lowers the oxygen content in the melt by the synthesis of MgO so that the nitridation reaction of aluminum is enhanced. The dispersion of the reinforcement has been found to be improved for longer injection times, as well as the particle size -1-3  $\mu\text{m}$  for 1 h vs. sub-micron AlN for 2 hours. Ammonia has shown to cause a massive increase in porosity especially in the middle/bottom part of the casting. This is possibly due to the entrapment of hydrogen in the melt once the AlN are formed on the top and the metal viscosity increased. Silicon effects on the nitridation reaction have also been studied. The formation of magnesium silicide phase  $\text{Mg}_2\text{Si}$  suppresses the synthesis of MgO and thus, of AlN. This suggests that aluminum nitrides might form during cooling and not at high temperatures, since  $\text{Mg}_2\text{Si}$  starts to precipitate at around 600-650  $^\circ\text{C}$ .

#### References

[1] Dr. Alois Franke, "Franke Keynote", Summer School 28 July- 1 August 2008, Worcester Polytechnic Institute, Worcester, MA.

- [2] A.Kelkar, R.Roth, J.Clark, " Automobile Bodies: Can Aluminum Be an Economical Alternative to Steel?", Journal of Materials, Vol 53 (2001), pp.28-32.
- [3] C.E.Freese, "Light-Duty Diesel market potential in North America, Diesel Engines Emissions Reduction Conference", August 22 2005, Chicago
- [4] F.Avella, "Le nuove tecnologie per la riduzione delle emissioni degli autoveicoli", Convegno Nazionale sul Particolato Atmosferico, Universita' di Milano-Bicocca, 12-14 Maggio, 2004.
- [5] <http://www.metalprices.com/>
- [6] F.S.Silva, "Fatigue o Engine Pistons – A Compendium of case studies, Engineering Failure Analysis", Vol.13 (2006), pp.480-492.
- [7] D.B.Miracle, "Metal Matrix Composites – From science to technological significance",Composites Science and Technology, Vol.65 (2005), pp.2526-2540.
- [8] Z.Ren and S.Chen, Mechanical properties of nanometric particulates reinforced aluminum composites, <http://www.materials.unsw.edu.au/NanoWeb>

**APPENDIX A**  
**Manufacture of Aluminum**  
**Nanocomposites:**  
*A Critical Review*

**Manufacture of Aluminum Nanocomposites:**  
*A Critical Review*  
**C. Borgonovo, D. Apelian**

---

*Abstract*

In the last twenty years, metal matrix nanocomposites have encountered a massive development. This paper reviews the research opportunities of these materials and their application markets. Particulate-reinforced nanocomposites have been extensively employed in the automotive industry for their capability to withstand high temperature and pressure conditions. Several manufacturing methods have been used to fabricate them. A not homogeneous particle dispersion and a poor interface bonding are the main drawbacks of conventional techniques. The distinction between ex-situ and in-situ processes will be provided. In-situ techniques -where the secondary phase is formed directly in the melt- don't show the shortcomings of conventional fabrication routes. The category of in-situ gas/liquid processes is investigated. The thermodynamics and kinetics of the reaction between the precursor gas and the liquid metal have been analyzed and their role on particle formation studied.

## *Contents*

1. Metal-matrix composites in context
  - 1.1 Nano-particles reinforced composites
2. Critical issues in nanocomposites
  - 2.1 Uneven dispersion and agglomeration
  - 2.2 Interface de-bonding
3. Manufacturing routes
  - 3.1 State of art
  - 3.2 Ex-situ methods
    - 3.2.1 Solid state
    - 3.2.2 Liquid state
  - 3.3 In-situ methods
    - 3.3.1 In-situ versus ex-situ
4. Gas-liquid interaction for the manufacturing of aluminum based nanocomposites
  - 4.1 Introduction
  - 4.2 Thermodynamics of the gas-liquid process
    - 4.2.1 The role of magnesium
  - 4.3 Kinetics of the gas-liquid process
5. Concluding remarks

*References*

*Table of figures*

## 1. Metal-matrix composites in context

Metal-matrix composites are a hybrid material in which rigid ceramic reinforcements are embedded in a ductile metal alloy matrix. They tailor the best properties of two different materials, such as ductility and toughness of the metallic matrix and the high modulus and strength of ceramic reinforcements. Their first application can be traced back to the late 1960s, with the development of a steel-wire reinforced copper alloy [1]. The aerospace industry was the first one to apply the technology of composite materials to spacecrafts components. High-performance materials are a necessity when the environment is extreme and critical, as experienced in space missions. It is worth mentioning that the International Space Station, during its life, will undergo 175,000 thermal cycles from +125 C° to -125 C° as it moves in and out of the Earth's shadow. During the last 4 decades, aluminum matrix composites were specifically developed to meet both aerospace and defense needs. Continuous boron fiber reinforced aluminum was used in the Space Shuttle Orbiter as the frame and rib truss members in the mid-fuselage section; there are other applications such as landing gear drag link yielding 45% weight saving. A Gr/Al composite is the constituent of a high-gain antenna boom for the Hubble Space Telescope. This boom (3.6 m long) offers the desired stiffness to maintain the position of the antenna during space maneuvers.

In the 1980's and early 1990's, metal matrix composites development programs were in vogue and there was much activity at all major aluminum producers. Alcan, through its Duralcan subsidiary, established a 25 million pound per year production capability for particulate-reinforced aluminum composites. The Aluminum Association convened the Aluminum Metal Matrix Composites Working Group, a product of which was the ANSI H35.5 standard that established a nomenclature system for aluminum composites [2]. As expected, metal matrix composites found applications in a variety of other markets such as automotive, electronic packaging, industrial product and recreational products [3]; some of these are:

- Chevrolet Corvette and GM S/T pick-up truck drive shafts
- Plymouth Prowler brake rotors and GM EV-1 brake drums
- Toyota diesel engine pistons
- Pratt & Whitney 4000 series engine fan exit guide vanes
- Motorola's Iridium Satellites and GM EV-1 electronic packaging applications
- F-16 fighter aircraft ventral fins and fuel access covers
- Bicycle components and golf clubs

The compelling need for vehicles with low fuel consumption is pushing the automotive industry to turn to composites as an engineering pathway for a sustainable future. An almost 70% increase of metal matrix composites is estimated to take place in the use of Al in vehicles from 2004 to 2013, see Figure 1. Though metal matrix composites offer many advantages, they do have shortcomings such as low fracture toughness and machinability.

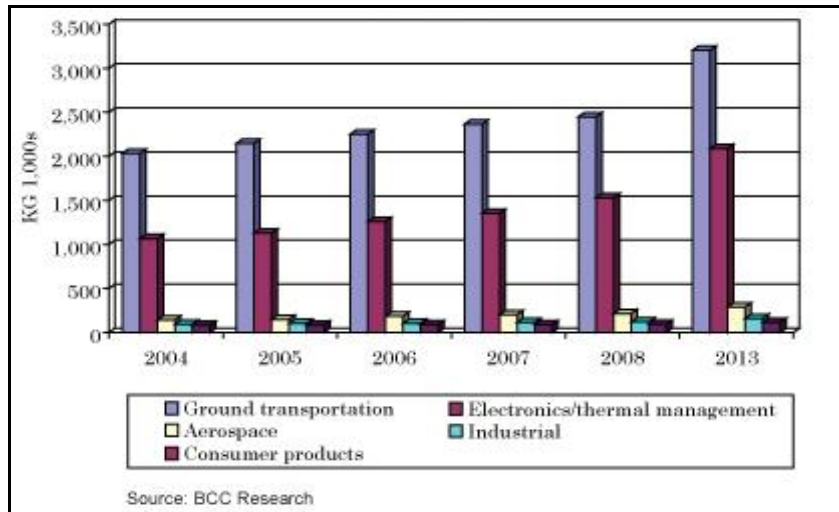


**Figure 1: Global outlook of metal-matrix composites by application segment (2004-2013)**

Nanocomposite metal-matrix materials have emerged as a viable alternative to overcome the limitations of metal matrix composites; however nanocomposites are challenging to produce as structural components due to difficulties in attaining a homogeneous distribution of the nanophased particles. Nanocomposites are reported to be the material of the 21<sup>st</sup> century; nanotechnology really came into being in 1959, when Richard Feynmann presented "There's Plenty of Room at the Bottom". Since 1959 nanotechnology has grown dramatically. In 2004, the American Ceramic Society defined Nanotechnology as: *"The creation, processing, characterization, and utilization of materials, devices, and systems with dimensions on the order of 0.1–100 nm, exhibiting novel and significantly enhanced physical, chemical, and biological properties, functions, phenomena, and processes due to their nanoscale size"*. Representative metal nanocomposite systems and associated attributes are given in Table 1 [4]:

<b>Matrix/Nano-sized Reinforcement</b>	<b>Properties</b>
Al/SiC      Mg/SiC Al/Al <sub>2</sub> O <sub>3</sub> Mg/Al <sub>2</sub> O <sub>3</sub>	<i>Improved ultimate strength, hardness and elastic modulus</i>
Al/AlN	<i>Higher compression resistance and low strain rate</i>
Ni/PSZ and Ni/YSZ	<i>Improved hardness and strength</i>
Cu/Al <sub>2</sub> O <sub>3</sub>	<i>Improved microhardness</i>

**Table 1: Metal nanocomposite systems of interest and associated attributes [4]**

## 1.1 Nano-particle reinforced composites

Nano-particles have progressively replaced other discontinuous reinforcement structures such as nano-fibers, nano-wires or nano-platelets. SiC, TiC, WC, TaC, TiB<sub>2</sub>, AlN, and Al<sub>2</sub>O<sub>3</sub> are some of the most common types of nano-particles that have been utilized. The characteristics of nano-particle reinforced composites can be summarized as follows:

- drastic change of fracture mode from inter-granular fracture of monolithic metal to trans-granular fracture of nano-composites;
- moderate to significant improvement in strength;
- moderate improvement of fracture toughness;
- significant improvement of creep resistance, thermal shock resistance, and wear resistance;
- significant enhancement of dimensional stability at high temperatures.

Zebarjad et al. [6] compared the effect of 25 μm, 5 μm, and 70 nm SiC particles on dimensional stability in an aluminum alloy. The temperature sensitivity of aluminum decreases in the presence of both micro and nano-sized silicon carbide, though the effect of nano-sized silicon carbide on dimensional stability is much higher than that of micro-sized ones. Ren and Chan [7] added SiC nano-particles (50 nm) to 7075 aluminum alloy. They pointed out increased wear resistance and high temperature creep resistance when comparing to the same alloy reinforced with 13 μm SiC particles. Furthermore, the volume percentage of nano-particles needed to achieve this result was considerably smaller than micro-particles volume percentage. Again, the tensile strength of an aluminum alloy reinforced with 1 % volume of Si<sub>3</sub>N<sub>4</sub> (10 nm) has been found to be comparable to that of the same alloy reinforced with 15 % volume of SiC particle in the micro-size range (3.5

μm), with the yield strength of the nano-metric composite being significantly higher than that of the micro-metric [8]. The existence of a threshold size ("critical size") below which the addition of particles improves properties has been reported (Table 2) [4]. It must be noted that the mechanism responsible for property improvements remains a matter of debate among researchers.

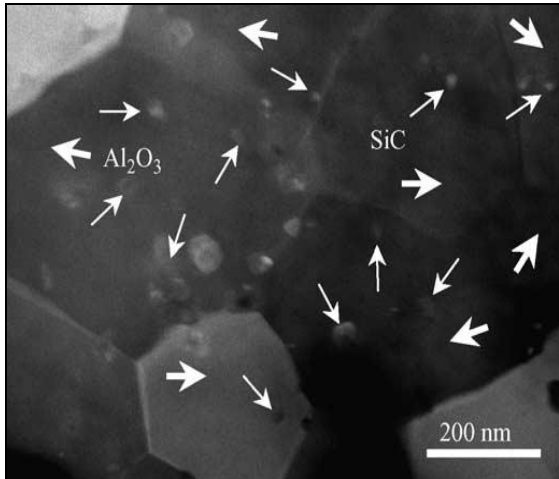


**Figure 2: TEM image of nano-particles embedded in aluminum grains [5]**

<b>Properties</b>	<b>Critical Reinforcement size (nm)</b>
Catalytic activity	<5
Softening of hard magnetic materials	<20
Change of refractive index	<50
Producing electromagnetic phenomena such as super paramagnetism	<100
Strengthening and toughening	<100
Modifying hardness and plasticity	<100

**Table 2: Critical size for properties improvement [4]**

Strengthening theory based on a continuum approach is not useful; since it ignores the influence of particles on micromechanics of deformation - i.e., location of particles, grain size, and dislocation density. Several discontinuous approaches have been formulated to include the particle effect. The modified shear lag theory [10,11] of Nardone and Prewo, the Eshelby-based particle-compounded model and the EMA (effective medium approximation) model by Stroud are the most popular ones [11]. They take into account one or more of the following strengthening mechanisms:

- *Orowan mechanism*: the stress that must be applied to force a dislocation to by-pass an obstacle (such as a particle) is at the base of the Orowan strengthening effect, which is really the resistance of closely spaced hard particles to the passing of dislocations. If the particles are coarse (in the micro-size range) and the inter-particle spacing is large, the Orowan effect is not significant [10]. Instead, when highly-dispersed nano-sized particles are present in a metal matrix, Orowan strengthening becomes more favorable. Creep resistance and thermal stability are consistently enhanced, even for only a small volume fraction (<1%), due to the fact that bowing is necessary for dislocations to bypass the particles. In addition to this, TEM (transmission electron microscope) observations reveal

strong dislocation bowing and tangling around the particles themselves, further confirming what stated above [9,10,11].

- *Thermal mismatch:* matrix and reinforcement have different coefficients of thermal expansion. Therefore, during the cooling process, plastic deformations are produced in the matrix at the interface. These deformations can cause defect such dislocations. Due to the increment of interfacial area, the density of dislocation is also increased [11].
- *Load-bearing:* the strong bond due to the cohesion between particle and matrix contributes to carry the load applied to the material [10,11].

When all these factors are taken into account, the increase in mechanical properties with the decrease in size can be estimated.

## 2. Critical issues in nanocomposites

There is still uncertainty in theoretical modeling and experimental characterization of nano-scale reinforced materials. The main challenges are related to the processing method and pertain the capability to disperse the secondary phase in the matrix, as well as the achievement of a strong interfacial bonding. Most fabrication processes are unable to fulfill these tasks. Clusters of particles and weak matrix-reinforcement interfaces compromise the ability of the composite material to function under highly rated conditions, such as high temperature and pressure typical of automotive applications.

### 2.1 Uneven dispersion and agglomeration

Agglomeration is a common phenomenon that occurs when a solid particle comes into contact with a non-wetting medium [12,13]. The clustered particles significantly reduce the failure strain of the composite, the degradation is attributed to preferential nucleation of cracks in clustered regions and final fracture is produced by crack propagation through the matrix to other clusters. Clustering occurs due to combined effect of agglomeration, sedimentation (particle settling rate) and particles pushing by the advancing solid-liquid interface. The tendency to form particle clusters can be explained based on the principle of the minimum Gibbs free energy for the system. A solid inclusion is never perfectly smooth: its surface is covered with cavities filled with gas, which contribute to increase the Gibbs energy of the system. This is clear when the equation defining the Gibbs energy of a gas-liquid-solid system is analyzed [12]:

$$\Delta G = (\mu G(T, P) - \mu L(T, P)) + \gamma_{LG} \Delta S_{LG} + \gamma_{SG} \Delta S_{SG} + \gamma_{SL} \Delta S_{SL} \quad (2.1)$$

where  $T$  is the temperature,  $P$  the pressure in the liquid,  $\mu_G$  and  $\mu_L$  the chemical potentials of gas and the liquid,  $\Delta S$  is the change in interfacial areas and  $\gamma$  surface energies. When the particle size is brought down to the nano-scale range, surface energy is enhanced by three orders of magnitude (Table 3), introducing strong instability in the system and hindering particle wetting by the molten metal.

Particle size (cm)	Total surface area (cm <sup>2</sup> )	Surface energy (J/g)
0.1	28	$5.6 \times 10^{-4}$
0.01	280	$5.6 \times 10^{-3}$
0.001	$2.8 \times 10^3$	$5.6 \times 10^{-2}$
$10^{-4}$ (1 $\mu\text{m}$ )	$2.8 \times 10^4$	0.56
$10^{-7}$ (1 nm)	$2.8 \times 10^7$	560

**Table 3: Variation of surface energy with particle size (1 g of sodium chloride) [15]**

The natural tendency towards equilibrium is the spring that allows the system itself to assume a physical configuration for which the Gibbs energy is lowered to a minimum value. Under this optic, agglomeration acts like a "stability configuration": several nano-particles cluster in one micro-agglomerate -Figure 3b-, providing a less extended total interfacial area -Figure 3a-. The dynamics of the relative motion of two nano-sized particles has been extensively studied [13,15]. Due to the complexity of the problem, the analysis is usually limited to two main mechanisms: Brownian diffusion or perikinetic aggregation and inter-particle forces (electrostatic and Van der Waals). External forces are not considered and particle inertia is neglected.

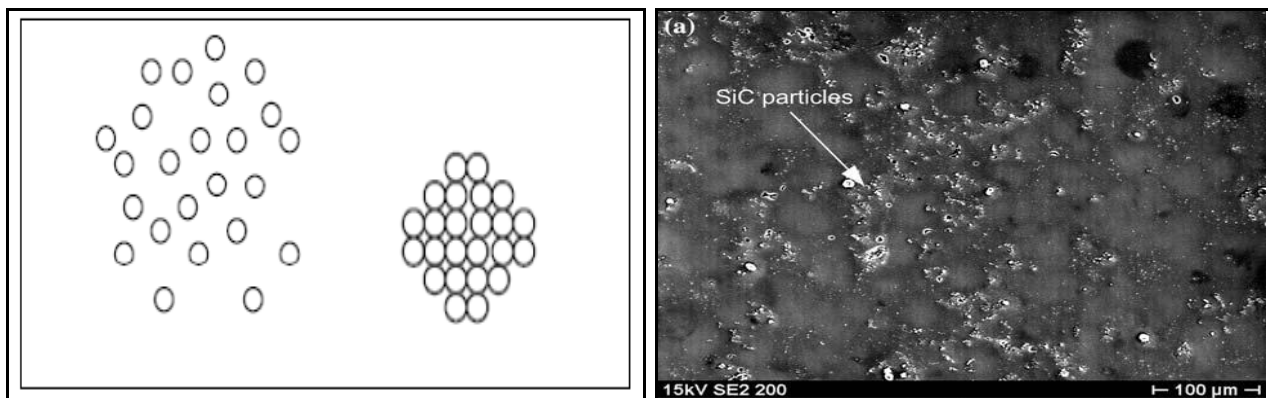


**Figure 3: a) Loose and clustered particles. The interfacial area is reduced in the cluster; b) Clusters of SiC nano-particles [14]**

## *Brownian motion*

Brownian diffusion, usually referred to as fast aggregation limit [14], ensures the continuous collision between particles. It can be defined as the incessant random motion exhibited by microscopic particles immersed in a fluid. It has been demonstrated [13] that a suspended particle is randomly bombarded from all sides by thermally-excited molecules coming from the liquid. A. Einstein noticed that if one solid inclusion is small enough to behave like a gas molecule, it is continuously hit by the liquid molecules and displaced as a consequence. The magnitude of the displacement follows a Gaussian statistic distribution according to the relation:

$$d = \sqrt{\frac{2kTt}{6\eta\pi r}} \quad (2.2)$$

where  $\eta$  is the viscosity of the medium,  $t$  the time,  $r$  the particle radius,  $T$  the temperature and  $k$  the Boltzmann's constant. The displacement increases with decreasing particle radius, thus enhancing the probability of a collision to occur. It has been confirmed [13] that for particles smaller than 3.5  $\mu\text{m}$ , Brownian motion totally dominates the agglomeration dynamics. The aggregation rate for 20 nm particles has been evaluated to be four order of magnitude higher when compared to particles in the range of 1  $\mu\text{m}$  [15]. This behavior can be explained by considering that, as the particle size increases, the potential energy of repulsion increases, thus making aggregation less likely.

## *Inter-particle forces: Van der Waals attraction and electrostatic repulsion*

Van der Waals in 1873 stated that the non-ideality of gases can be attributed to the existence of molecular or atomic interactions. Such dynamics interactions are established between the instantaneous dipoles formed in the atoms by their orbiting electrons. Thus, the resulting force is weak and becomes significant only at a short particle distance. Hamaker [16] in 1937 found such interactions to exist also between particles and modified the formulation of Van der Waals through the so called "additivity concept" (single atoms or molecules make up the particle). When the cavities located on a solid inclusion are filled with gas, negative Van der Waals forces come into play, causing particle agglomeration. Attraction is favorable because it contributes to reduce Gibbs free energy of the amount:

$$\theta = \frac{-Ar}{12H^2} \quad (2.3)$$

where  $A$  is the Hamaker constant, which depends on the polarization properties of the molecules on the particle surface,  $r$  is the reduced particle radius and  $H$  the inter-particle distance [13]. When particle dimension is smaller than  $1\ \mu\text{m}$ , Van der Waals forces dominate. Coulomb force of repulsion competes with Van der Waals attraction. It can be noted from Figure 4 that the electrostatic repulsion is overcome by the Van der Waals attraction force for a inter-particle distance down to  $1\ \text{nm}$ . For smaller values the Born repulsion of adjacent electron clouds dominates.

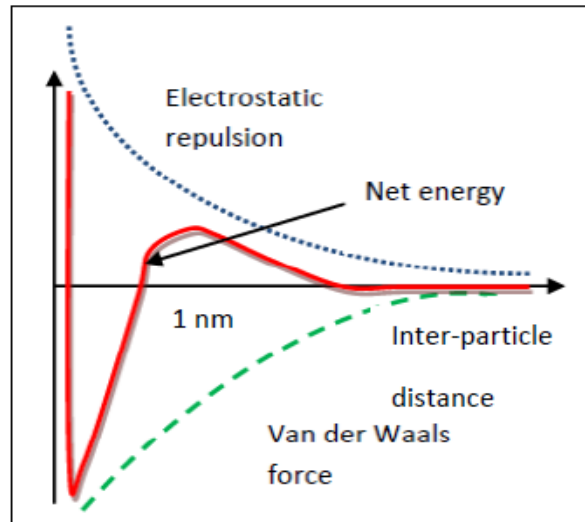
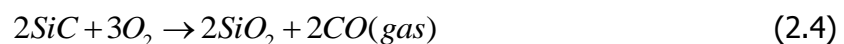


**Figure 4: Forces acting between two particles [15]**

## 2.2 Interface de-bonding

The interface bonding between particles and matrix must be good. This is essential for an effective load transfer from the matrix to the particle and for delaying the onset of particle–matrix de-cohesion, both of which have a profound effect on the strength and stiffness of the composite. Oxide layers on the surface of the particle increase tremendously the surface energy, thus wettability is decreased and floating enhanced. Surfaces of SiC particles are frequently covered with  $\text{SiO}_2$  layers [17,18]. Such layer originates during the SiC production process: below  $1200^\circ\text{C}$ , SiC can undergo passive oxidation in which  $\text{SiO}_2$  film forms, according to the reaction:



It's difficult to determine whether oxides are responsible for this unsatisfactory bonding. Exposure of bare particles on the fractured surface can provide information in this sense. Figure 5 shows a fractured surface where the crack coincides with segregation of SiC nano-particles. The particles are weakly bonded to the matrix and EDS analysis confirm the presence of oxides on their surface –Figure 6.

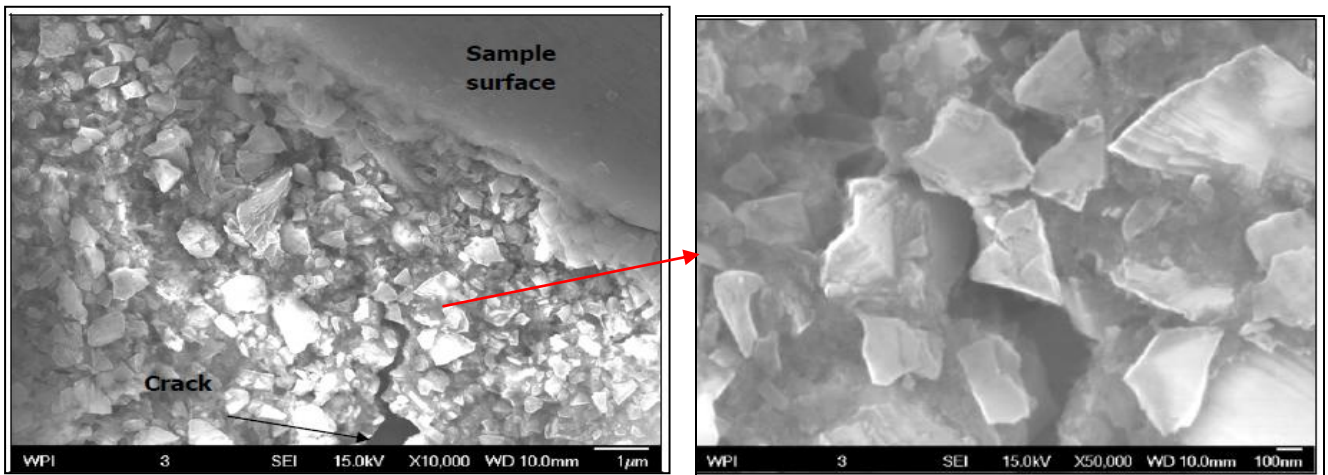


**Figure 5: SiC nano-particles on A356 aluminum alloy fractured surface**

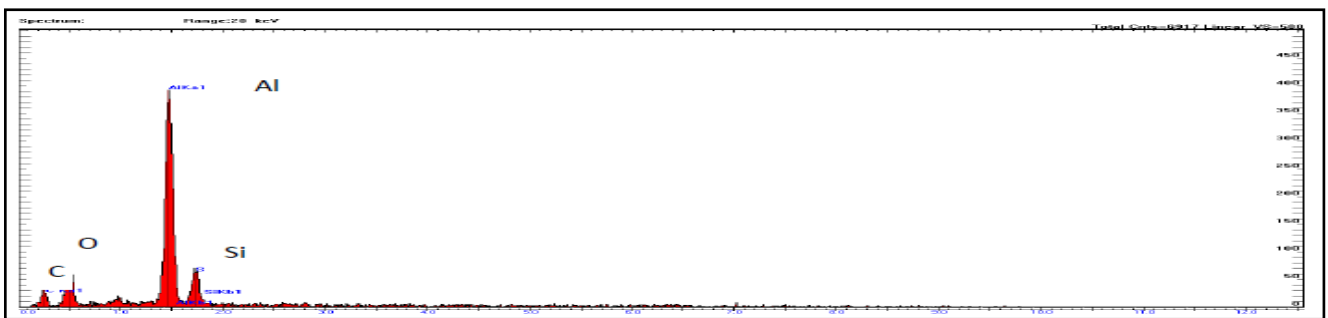


**Figure 6: EDS spectrum of a SiC nano-particle on the fractured surface**

### 3. Manufacturing routes

#### 3.1 State of art

According to the manufacturing process, metal matrix composites can be divided into ex-situ and in-situ. When the reinforcement is externally added to the matrix, ex-situ composite materials are created. In situ synthesizing of metal matrix composites involves the production of reinforcements within the matrix during the fabrication process. Ex-situ manufacturing techniques can be further grouped into solid state, liquid state and semi-solid processing. Among solid state techniques, powder metallurgy and mechanical attrition are the most popular ones. The nano-scale can be easily reached, although the cost of the powder is significantly high. Interfacial and surface wetting issues are considerably diminished. This is because both phases remain in the solid state, where diffusivity is much lower [19,20]. The final products are generally affected by a high amount of porosity, which strongly decreases the fatigue resistance and requires further metal working. Also, when the process involves attrition at high temperatures, chemical modification of the initial constituents is likely to happen [21,22]. Liquid state routes can be sorted into four major categories: infiltration, agitation, spraying and ultrasonic cavitation based solidification. Semi-solid processing involves electromagnetic stirring and semi-solid casting. Liquid metal is generally less

expensive and easier to handle than powders, and the shape flexibility constitutes a significant advantage. Liquid state processes are generally fast and easy to scale-up. Despite this, they are affected by the lack of wettability of the reinforcement and by interfacial reactivity. Moreover, they are often limited to low-melting point metals [19,20]. In-situ metal matrix composites are not affected by the shortcomings typical of ex-situ composites, although control of process variables still remains an issue. In-situ fabrication methods can be divided into two major categories according to the physics of the process itself:

- “Reactive” routes: the reinforcement is synthesized within the metal matrix through a gas-liquid, liquid-liquid, or solid-liquid reaction.
- “Morphological” routes: a favorable composite architecture evolves as a consequence of processing. Deformation processes and directional solidification of eutectics alloy belong to this category.

The features of ex-situ techniques and their drawbacks will be discussed in the following paragraph. In addition to this, the advantages of in-situ composites will be illustrated and the most popular in-situ methods described.

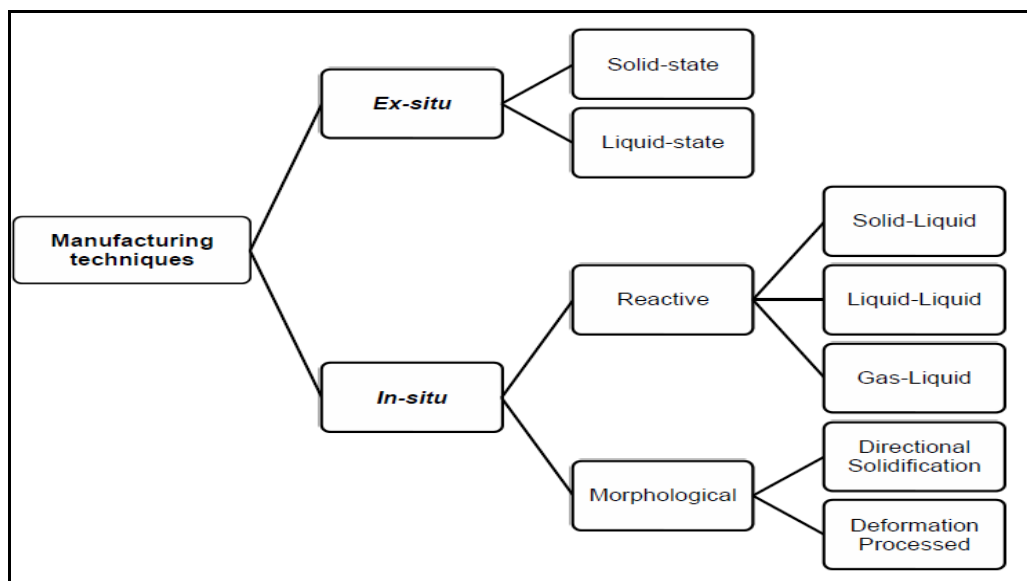


**Figure 7: Manufacturing methods for metal-matrix nanocomposites**

## 3.2 Ex-situ methods

### 3.2.1 Solid-state

#### *Powder metallurgy*

Most of prior work in synthesizing nanocomposites involves the use of powder metallurgy techniques, which are usually affected by high costs. Blending of matrix and reinforcement powders followed by hot or cold pressing and sintering is a standard fabrication sequence. A schematic of a typical powder metallurgy procedure is shown in Figure 8. In the majority of powder metallurgy process, agglomeration can be minimized only if the size of the matrix powder is close to the size of the reinforcement phase. In addition to this, further working of products attained via powder metallurgy may cause the reinforcement phase to break up and deform the surrounding matrix, leading to stress concentration and cracking [23]. The advantages of the process are flexibility and near-net shape products. Moreover, the size range of metal powder offered by the market is very wide and can meet the needs of different purposes. Powder metallurgy has been used [8] to add 50 nm alumina particles to aluminum powder. The process consists in wet mixing (aluminum powder mixed with varying volume fraction of  $\text{Al}_2\text{O}_3$  powder in a pure ethanol slurry), followed by drying at 150 °C and cold isostatic pressing to compact the powder. The compacted powder is then vacuum sintered at 620 °C (approximately 60 °C below the melting temperature of aluminum). Massive clustering has been observed, and its occurrence increases with decreasing particle size. Ma et al. [24] fabricated via powder metallurgy nanometric silicon-nitride reinforced aluminum composites. They reported the presence of several agglomerates in the aluminum matrix. Peng et al. [25] created a novel and simplified process for producing aluminum matrix nanocomposites reinforced with oxide particles. The novelty lays in the use of  $\text{Al}_2\text{O}_3$  surface layers existing on matrix aluminum particles as the ceramic reinforcement. A good distribution has been achieved, although the process does not allow a satisfactory control of the phase of layers break-up and spreading. Moreover, the effectiveness and the scalability of the method have not been proved yet.

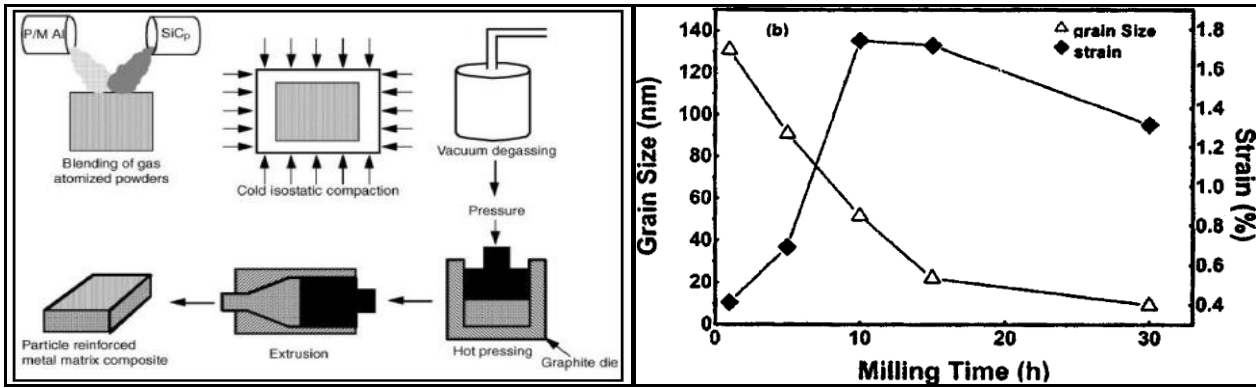


**Figure 8 Powder processing, hot pressing, and Figure 9: Grain size and strain vs. milling extrusion process for particulate reinforced composites [23] time for WC particles [26]**

### *Mechanical attrition and alloying*

Mechanical alloying was invented in 1980 to manufacture particle strengthened metal alloys. In the last ten years, the method of high-energy milling gained a lot of attention as a non-equilibrium process able to produce nano-scale microstructures. A variety of ball mills have been developed for different purposes including tumbler mills, attrition mills, shaker mills, vibratory mills, planetary mills [27]. In the high-energy ball milling process, alloying occurs as a result of repeated breaking up and welding of matrix and reinforcement particles. Both powders are subjected to severe plastic deformation due to the collision with the milling tool. Deformation occurs at high strain rate; thus, after extended milling –Figure 9-, the average powder grain size can be reduced to few nanometers [27,26]. It is worth mentioning that aluminum nanocomposites with the trade-name DISPAL, reinforced with  $Al_4C_3$  particles, have been manufactured via mechanical alloying [8]. Flexibility and scalability are points of strength of the process. It should be noted that contamination by the milling tool and the atmosphere may occur. Milling of refractory metals (tungsten) in a high-frequency shaker for extended times can result in iron contamination of more than 10 at.% [25]. To prevent these phenomena, the process has to be carried out in an inert atmosphere and the mills coated. Another major issue is the occurrence of chemical reactions as a consequence of the conversion of mechanical into thermal energy [27]. Zhang et al. [28] proved that there exists a particle size below which further size reduction can't be performed, since the stress necessary to break the particles is above the process capabilities. Such stress can be expressed as:

$$\sigma_f = \frac{K_c}{\sqrt{\pi a_c}} \quad (3.1)$$

Where  $\sigma_f$  is the fracture stress,  $K_c$  the fracture toughness and  $a_c$  size of material defects. When the particles are reduced to the nano-range, the likelihood of having internal defects and surface notches are considerably reduced. In this case,  $\sigma_f$  will approach the theoretical strength of the ceramic material. The impact stress of silicon-carbides is over 15 GPa, which is the value to be adopted to fracture a "perfect" (with no defects) ceramic. Such stress is not achievable with a conventional high energy mechanical mill. In addition to this, nano-particles produced by attrition have a not uniform size distribution and the process is limited to materials with very poor thermal conductivity [29].

### 3.2.2 Liquid-state

#### *Mechanical stirring*

Stir casting, suitable to disperse micron-sized particles, has been found to perform poorly when nano-particles are added to the metal matrix. The process restraints are:

- Particle introduction in the melt;
- Particle clustering;
- Weak bond between matrix and reinforcement

Because of the increase in surface area together with the reduction in particle size, insert the particles in the melt and homogeneously disperse them is challenging. The increase of interfacial energy raises the free energy of the system, causing agglomerates to form in order to re-establish the stable state –see paragraph 2-. Several stirring means have been developed to improve the dispersion. Ultrasonic based solidification has been the most successful one. The capability of rapidly and inexpensively producing large near-net shape components is the engine that pushes the research to make the process suitable to manufacture nano-composites.

#### *Ultrasonic cavitation based solidification*

High-intensity ultrasonic waves (above 25 W/cm<sup>2</sup>) can generate strong non linear effects in the liquid such as transient cavitation and acoustic streaming [30]. They produce a dispersive effect ideal to homogenize the microstructure of the composite material [31]. In order to benefit from such effect, an ultrasonic probe has been immersed into the melt to create the acoustic field – Figure 10- and nano-sized particles have been added during the ultrasonic process.

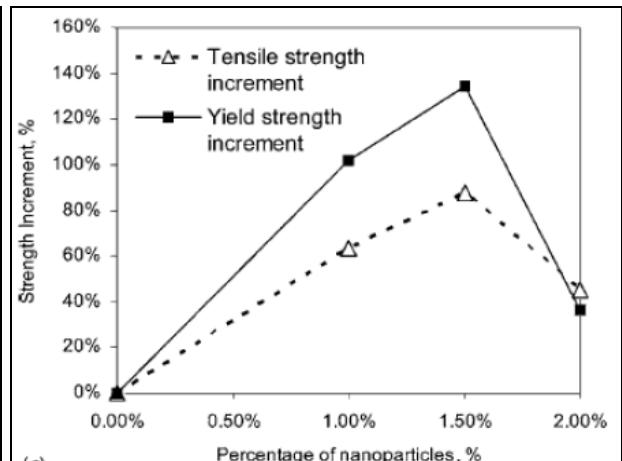
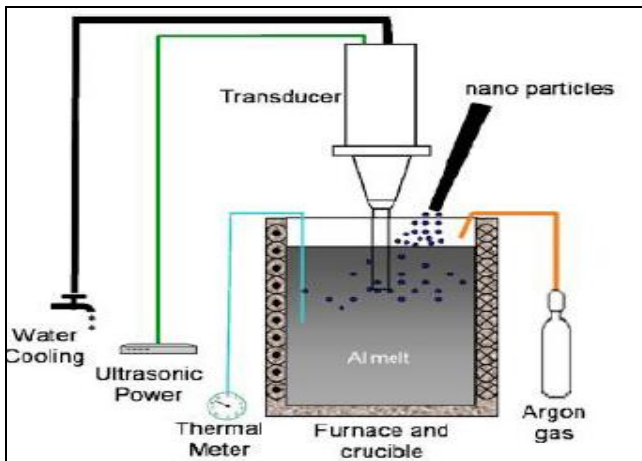


**Figure 10: Schematic of ultrasonic solidification [30,31]**

**Figure 11: Strength vs. nano-particles percentage**

The acoustic bubbles burst, creating hot micro-spots that locally raise the temperature of the melt. This enhances particle wettability and thus, favors a good dispersion. It has been measured [30] that with a 3.5 kW ultrasonic power, the ultimate strength and yield strength were improved more than 60% and 100% -Figure 11-. In addition to this, 2.0 vol% SiC nano-particles improve hardness by 20% [32].

### *Infiltration*

Infiltration consists in a porous "perform" (the reinforcement) whose pores are filled with liquid metal. Capillary forces hinder wetting of the ceramic reinforcement by molten metal and viscous drag through perform interstices. Evans et al. [20] observed from an "energetic" standpoint, metals generally do not bond to non-metals. One therefore cannot simply "place" the metal in contact with the ceramics material. The chemistry of the system must be modified, or an external pressure must be applied to force the contact between metal and particles and enhance wettability. Chemical modification includes coating, adding special elements to the matrix, or using special atmospheres. Unwanted phases have been traced in the matrix as a consequence [33,20]. When a mechanical force is used, the chemical composition remains unvaried, while porosity is reduced and the interfacial bond improved. Pressures of around ten atmospheres are needed to drive the metal into 1  $\mu\text{m}$  wide pores [20]. As a result, perform fragmentation, deformation and unevenly reinforced castings [33] are likely to occur. Since for nanocomposites very small pores must be infiltrated, heavy equipment is necessary to withstand the high pressure. Kaptay [34] noted that that when the partially infiltrated liquid metal reaches the "equilibrium depth" (the depth at which interfacial forces are zero), further infiltration will be ensured. According to this criterion, the pressure to apply is:

$$P_{threshold} = \frac{\pi}{R\sqrt{3}}(1.63\sigma_{lv} - W) \quad (3.2)$$

Where R is the particle radius, W the adhesion energy and  $\sigma_{lv}$  the interfacial energy between liquid and vapor. The lower the particle radius, the higher the threshold pressure. When pressures of some GPa are applied, nano-materials can be manufactured. Gierlotka et al. [35] used a toroid cell at pressures up to 7.7 GPa and temperatures up to 2000 °C for the infiltration of an alumina perform with grain size of 10 nm. The cost of a nano-dimension ceramic preform is industrially unaffordable.

### *Spraying*

The spray process is generally automated and quite fast. It is worth mentioning the Ospray process developed by Alcan International. Droplets of molten metal are sprayed together with the reinforcement and collected on a substrate where the composite solidifies [20]. Alternatively, the reinforcement can be directly placed on the substrate. An inert gas is used to atomize the molten metal. The process itself is relatively inexpensive, and the very high cooling rates provide a fine grain structure. Moreover, deleterious reaction products are generally avoided because of the short time the particles spend in the air [19]. Sometimes, if the deposition rate is higher than the solidification rate, liquid metal may be present at the surface of the substrate. Process control is hard to achieve, because of the numerous variables involved. Moreover, severe residual porosity has been observed [19, 33]. When injected is the spray stream, the secondary phase tends to surround the stream boundaries, causing inhomogeneous dispersion in the final piece [34]. This phenomenon is enhanced when nano-particles are employed. Equipment costs are very high and and large amounts of waste powder to collect and dispose are produced [19].

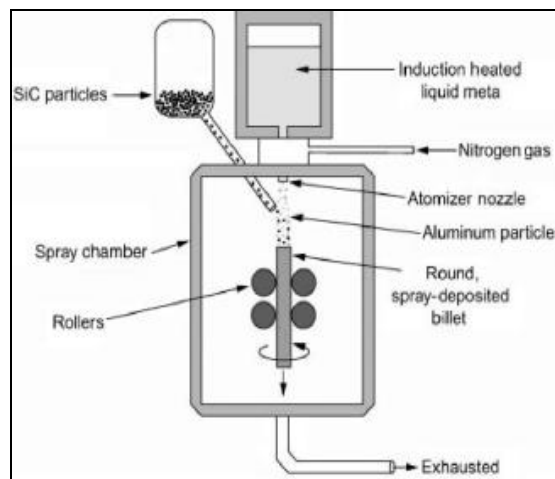


**Figure 12: Schematic of spraying process [34]**

### 3.3 In-situ methods

#### 3.3.1 In-situ versus ex-situ

When nano-composite materials are synthesized in-situ, fabrication issues typical of ex-situ techniques are eliminated:

- Thermodynamic incompatibility: interfacial reactions between the reinforcements and the matrix are likely to occur. Detrimental phases such as  $Al_4C_3$  and  $Ti_5Si_3$  have been detected in composite materials manufactured through mechanical stirring.
- Contamination: oxide layers around the particles cause an increase in surface energy, leading to a lack of wettability of the system [36].
- Inhomogeneous microstructure: particle agglomeration and clustering

The benefits that in-situ manufacturing methods provide are several [37,38]:

- Thermodynamically stability at high temperatures, allowing the development of aluminum alloys for high temperature applications;
- The interface between particle and matrix is clean, resulting in a strong interfacial bonding. Detrimental phases are eliminated and the creation of the nascent interface can be guided by process control. Wear resistance is enhanced as a result;
- Smaller particle size can be achieved and the improved distribution yields to superior mechanical properties;
- Widespread application field, ranging from the automotive market to the aerospace industry;
- Composites with a broad variety of matrix materials (aluminum, titanium, copper, nickel and iron) and reinforcing particles (borides, carbides, nitrides, oxides and their mixtures) have been produced;
- Low process costs.

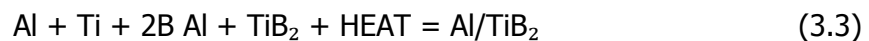
Commercial applications are still limited by the complexity of the reactions and the lack of knowledge concerning these techniques. In the next paragraph, the most popular reactive and morphological - see 3.1- in-situ processes are described.

### 3.3.2 Reactive processes: solid-liquid state

Elements or compounds react in the presence of a third liquid metallic phase that acts like a solvent medium. The reinforcement is generated via diffusion of components in the metal matrix [38]. Combustion synthesis, XD process, mixed salt reaction, direct metal oxidation and reactive synthesis are solid-liquid processes.

#### *Combustion synthesis*

Combustion synthesis is also known as self-propagating high-temperature synthesis (SHS) [33]; Merzhanov et al. [39] invented the process. A mixture of powdered elements is initially prepared and pressed into cylindrical pellets. Electrically heated coils or a laser act as the heat source that initiates a chemical reaction between the various elements. The solvent can be molten Al, Mg, Ti where other non metallic elements, such as C and B, are present. The ceramic compounds are burnt via ignition waves at a temperature higher than the melting point. A typical reaction is:



The highly exothermic nature of the process allows it to be self-sustaining and energy efficient. The heat released during the reaction keeps the propagation front stable by heating up the unreacted portion of the sample. The equipment is simple, processing times are short due to very high combustion rates (0.15 m/s) and metastable phases can be synthesized. In addition to this, volatile impurities are evaporated due to high temperature of the process. Although a variety of shapes and geometries can be attained, the high amount of porosity (up to 10%) in the final component still remains an issue. Further processing such as high-pressure consolidation is a necessary step.



**Figure 13: Combustion synthesis process**

### *Exothermic dispersion (XD process)*

The XD process has been developed by Martin Marietta Corporations and it has extensively applied to the manufacturing of light-weight materials. Jet engine turbine blades with a weight save from 30% to 50% have been fabricated with this process. It is a sustained high-temperature synthesis whose driving force is the difference of melting temperature between the components. Ceramic phases and a third metallic phase are put in contact and heated up above the melting point of the metallic phase. The ceramic phases release heat and interact, forming very fine (nano-sized) particulates [38,39, 40]. Particle size and distribution are system-dependent: they depend on the thermal conductivity of the environment and on the amount of heat developed during the reaction [39]. The volume percentage of reinforcement can be regulated by tailoring the composition of the initial species. The exothermic reaction eliminates oxides and provides clean interfaces [37, 39] Hot isostatic pressing of the final components is necessary in order to reduce the porosity level. A reinforcement size lower than 0.3  $\mu\text{m}$  has never been achieved via the XD process [37,38]. This could be due to the challenging control of the released heat and of the kinetics of the reaction [39].

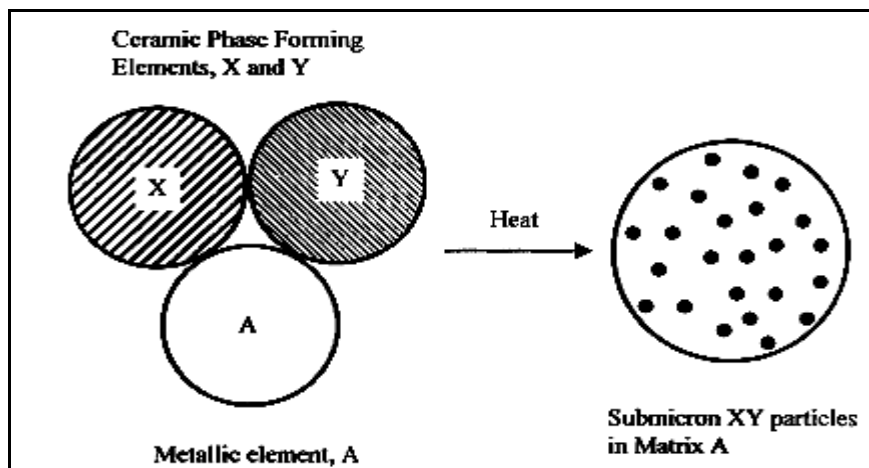


**Figure 14: XD process**

### *Mixed salt reaction (Flux-assisted synthesis)*

London and Scandinaviun Metallurgical Company developed the mixed salt reaction process. The basic concept comes from the purpose to produce grain refining aluminum alloys [38]. Mixed salts containing Ti and B with an atomic ratio in accordance with Ti/2B ( $\text{K}_2\text{TiF}_6$  and  $\text{KBF}_4$ ) are introduced into a stirred aluminum melt to form a fine dispersion. Pure Al and Al-Cu alloys reinforced with in situ  $\text{TiB}_2$  particles have been successfully manufactured. The sequence of the reaction is:



Chu et al. [41] added carbon-forming refractory materials to the molten metal and introduced fine carbon particles into the reactive salt. Large particles and areas characterized by an uneven dispersion have been observed. Chen et al. [42] observed that when the amount of the salt differs from the stoichiometric composition, needle-like, brittle phases (such as  $\text{Al}_3\text{Ti}$  needles) form in addition to the reinforcement. Despite the process is fast and easy to scale, it has several drawbacks. First of all, the slug produced by the salts must be taken out from the aluminum melt. Moreover, unwanted reaction products surrounding the particles could weaken the strength of the material and lower the reaction rate [43].

### *Direct metal oxidation (DIMOX)*

Lanxide Corporation developed the DIMOX process. It involves the oxidation of a liquid metal at very high temperatures -1700 K for aluminum alloys-. The reaction products start growing from the interface. Fresh liquid is continuously supplied in front of the interface by flowing through microchannels. Capillary forces are necessary to sustain the reaction: the ceramic preform must be continuously infiltrated by the oxidating molten alloy. The slow growth rate -1 mm/hour- limits the production rate of the process.

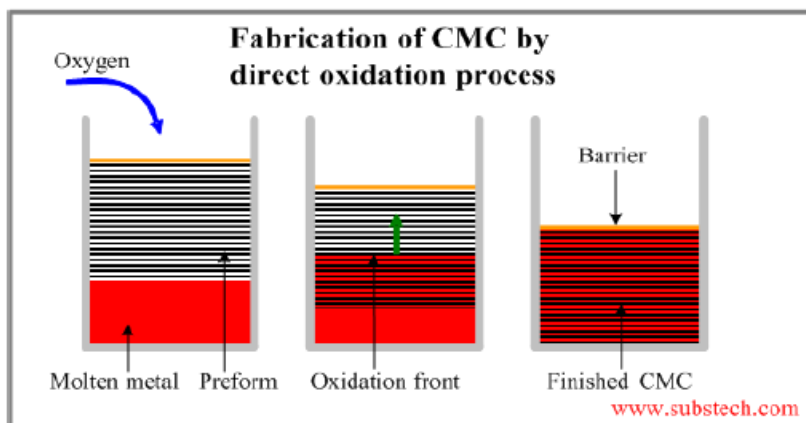


**Figure 15: DIMOX process**

### 3.3.3 Reactive processes: liquid-liquid state

The MixAlloy Process patented by Sutek Corporation [44] has been applied to manufacture nano-composite materials. Two streams of metal melts containing ceramic inclusions interact with each other in a reaction chamber to form refractory particles [37]. The mixture is then rapidly cast or atomized. Titanium boride particles in a copper matrix have been manufactured with this method. It has been pointed out [38] that particle sizes around 50 nm have been achieved. In the first process disclosure by Nam.P.Suh [44] the impingement between the metals is direct, while in a subsequent patent [45] the impingement is indirect. This way, instability in the metal streams are mitigated. A truly homogeneous mixing of the materials involved it's hard to ensure. The impingement itself may not be able to mix adequately the metal streams. In addition to this, unreacted elements have been detected, even though the Stoichiometry is locally maintained [45].

### 3.3.4 Morphological processes: directional solidification

Directional solidification has been firstly applied to manufacture nickel-based superalloys [46]. It was then extended to intermetallic eutectic compounds, such as titanium aluminides and nickel aluminides eutectic systems [33]. Such materials are commonly employed in the aerospace industry and specifically to manufacture gas turbine blades [33]. Several melting techniques have been employed, such as induction heating, thermal-gradient controlled solidification and electron beam heating. The Bridgeman method, despite it's a relatively old process, is still the most used [47]. Solidification starts from a seed placed at one side of the ingot and proceeds towards the other end of the ingot. When the Bridgeman method is employed, random interruptions resulting in discontinuities in the aligned eutectic reinforcement are absent. On the other side, contamination from the crucible material [33] often occurs. The composite components are thermodynamic stable and the microstructure can be controlled just by the adjusting the thermal gradient in front of the solidification front [40,46,48]. The shortcomings of these materials are low durability, low fracture toughness and low fatigue resistance especially at room temperature [44,49]. It is worth mentioning the existence of a "Japanese National project of application of eutectic composites for 1700 °C-class gas turbine". An innovative turbine nozzle and combustor panels made of directionally growth  $\text{Al}_2\text{O}_3/\text{YAG}$  have been developed. After 250 hours of high temperature exposure (1700 C°) no changes in microstructure and no reduction in flexural strength occurred -Figure 16-.

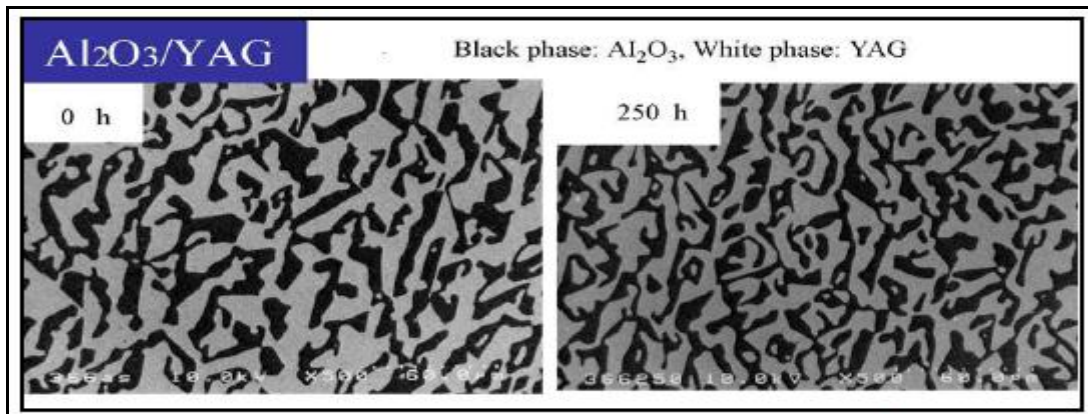


**Figure 16: Microstructure of the directionally solidified Al<sub>2</sub>O<sub>3</sub>/YAG after 0 and 250 hours at 1700 C°[49]**

Moreover, hot corrosion resistance and oxidation resistance were strongly enhanced as well as the power-to-weight ratio. In the patent [50], Zhao et al. illustrated the variety of intermetallics compounds that can be produced by direct solidification of nickel-based superalloys. Principally they are Ni<sub>3</sub>(Al,Ti,Nb,Ta) precipitates formed in situ in a nickel matrix containing also chromium, rhenium, molybdenum, cobalt and tungsten. They noticed an increase of yield strength of 50 ksi at 1100 C° , although other needle –like phases have been found. The composition of the growing phases must be strictly controlled in order to avoid harmful components. Bei et al. [46] noted the sensitivity of the process to the alloy composition. A regular morphology is more likely to occur for those systems whose phase diagram is symmetric with respect to the eutectic point. Morphology control is therefore the main issue, together with low production rates, the cost and the size of the equipment (Bridgeman furnace).

#### 4. Gas-liquid interaction for the manufacturing of aluminum based nanocomposites

##### 4.1 Introduction

The gas-liquid process belongs to the category of in-situ techniques. A gas is injected into the aluminum melt composed by one or more elements. Such gas reacts chemically with the melt and form the reinforcement phase. Refractory elements can also be added to the melt to tailor the precipitates. Table 4 shows gases, matrices and secondary phases that can be synthesized, together with the chemical reactions involved [51-57]. Tyagi et al. [58] manufactured aluminum nitrides with a diameter smaller than 1 μm, by bubbling ammonia gas in a Mg-Al melt. The temperature was kept at 900 C° and the gas was purged for 70 minutes with a constant flow rate. Shyu et al. [56] bubbled methane gas in Al-Ti melt to form TiC particles. The yield strength increased up to 18 % and the hardness by 20%. The size of the particles was smaller than 0.1 μm.

<b>Precursor gas</b>	<b>Matrix composition</b>	<b>Reinforcement phase</b>	<b>Chemical reaction</b>
N-bearing gas: N <sub>2</sub> , NH <sub>3</sub>	Pure Al, Al-Ti, Al-Si, Al-Mg, Al-Mg-Ti, Al-Mg-Si	AlN, TiN, TaN	$2\text{NH}_3 \rightarrow \text{N}_2 + 3\text{H}_2$ (1) $\text{Al(l)} + \frac{1}{2}\text{N}_2 = \text{AlN}$ (2) $\text{Al-Ti} + \frac{1}{2}\text{N}_2 \rightarrow \text{Al} + \text{TiN}$ (3) $\text{Al-Ta} + \frac{1}{2}\text{N}_2 \rightarrow \text{Al} + \text{TaN}$ (4)
C-bearing gas: CH <sub>4</sub>	Al-Ti, Al-Si	TiC, SiC, Al <sub>4</sub> C <sub>3</sub>	$\text{CH}_4 + \text{Ar} \rightarrow \text{C} + 2\text{H}_2 + \text{Ar}$ (5) $\text{Al-Si} + \text{C} \rightarrow \text{Al} + \text{SiC}$ (6) $\text{Al-Ti} + \text{C} \rightarrow \text{Al} + \text{TiC}$ (7) $\text{Al-Si} + \text{C} \rightarrow \text{Al-Si} + \text{Al}_4\text{C}_3$ (8)

**Table 4: Gas-liquid process gases, matrices, products and reactions**

The process is characterized by:

- Negligible costs. The gas is inexpensive and can be easily found on the market [51]. Commercial nano-particles are expensive. But this cost is eliminated since the particles are grown in the metal itself;
- No surface contamination that could affect the interfacial bonding;
- No detrimental phases. The thermodynamic of the process can be controlled to suppress the formation of unfavorable phases [52,51].
- Extremely homogeneous microstructure. The particles are naturally dispersed in the metal matrix [43].

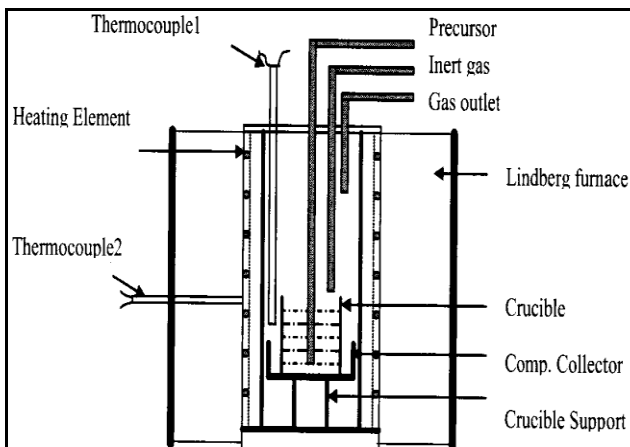


**Figure 17: Schematic of gas-liquid process [52]**

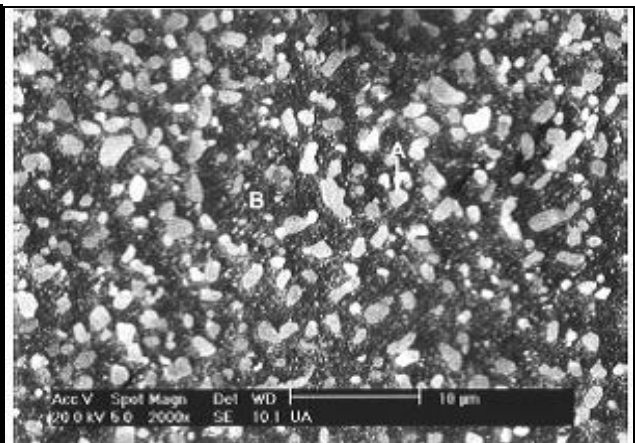


**Figure 18: AlN particles in Al matrix via gas-liquid process [51].**

Some limitations affect the process [56]:

- The temperatures necessary for the reaction to occur are very high (1300-1600 K depending on the gas and the matrix).
- The high apparent viscosity hinders the production of a high percentage of reinforcement.
- Process times are quite lengthy: around four hours totally (time to heat the melt at above 1300 K and for the bubbling process).
- The method is not applicable to materials with high melting temperatures.

## 4.2 Thermodynamics of the gas-liquid process

The choice of gas and matrix is dictated by the thermodynamics of the process. Gibbs energy change of the reaction indicates which system is more prone to the synthesis of the reinforcement. In addition to this, it determines the temperature range for the reaction to occur or to avoid detrimental phases. The precursor gas must dissociate into its constitutive elements in order to react with the melt.

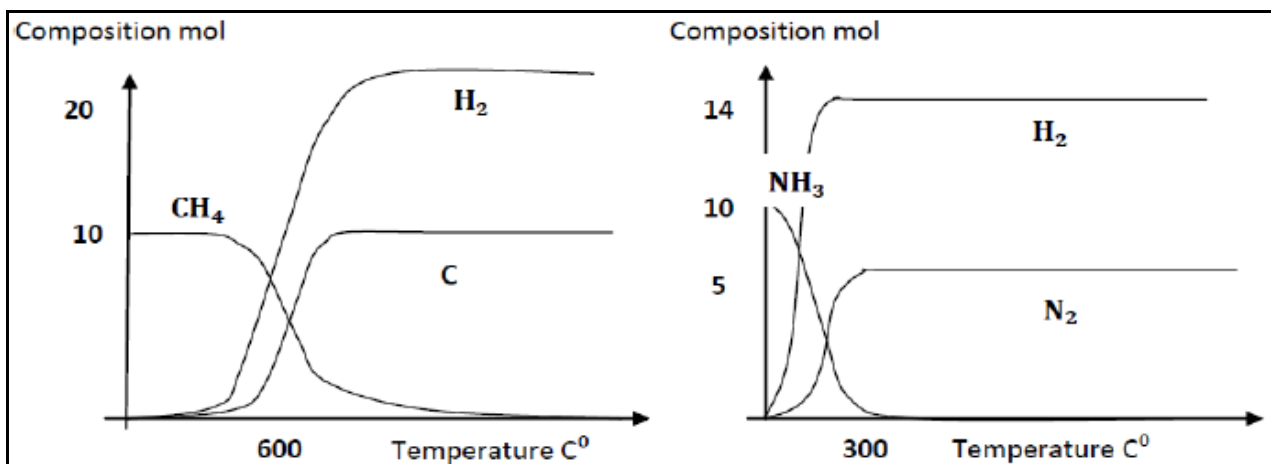


**Figure 19: Dissociation temperature for methane gas and ammonia gas [52]**

In Figure 19 it can be seen that methane gas starts dissociating at around 600 C°, while for ammonia gas the threshold temperature is 300 C°. This implies that for ammonia the reaction is thermodynamically favorable over a wider temperature range [52,53]. Unwanted phases such as  $Al_4C_3$  and oxides can also be predicted. For instance, reaction 6 and 8 in table 4 compete to determine the final products in Al-Si melts. The result is dictated by temperature, silicon content and activity coefficients of the components. An amount of silicon higher than 20 at.% suppresses

the formation of  $Al_4C_3$ . When nitrogen is the bubbling gas, the presence of oxygen obstacles the synthesis of aluminum nitrides. The minimization of the Gibbs free energy change establishes a limit of partial pressure and thus, of amount, for the oxygen in the melt. If the limit is overcome, then the reactions:



are more likely to occur than aluminum nitridation:



Commercial nitrogen has been employed and no nitrides detected in the microstructure. Therefore, commercial nitrogen gas has to be deoxidized in order to form AlN particles. On the contrary, when  $NH_3$  is bubbled, consistent aluminum nitrides are found [51]. In fact, hydrogen dissociates from  $NH_3$  functioning as oxygen getter and lowering its content in the reaction sites, thus increasing the permissible oxygen partial pressure -Figure 20-. Also, hydrogen may enhance the adsorption of  $N_2$  at the gas bubble-metal melt interface, thereby improving the rate of AlN formation. Zheng and Reddy [51] have deeply analyzed the kinetics of AlN formation in aluminum alloys melt. They found that the mean rate of forming AlN from ammonia is ten times the one of nitrogen. The amount of AlN attained is proportional to bubbling time, temperature, and gas flow rate, while it increases with diminishing tube nozzle diameter.

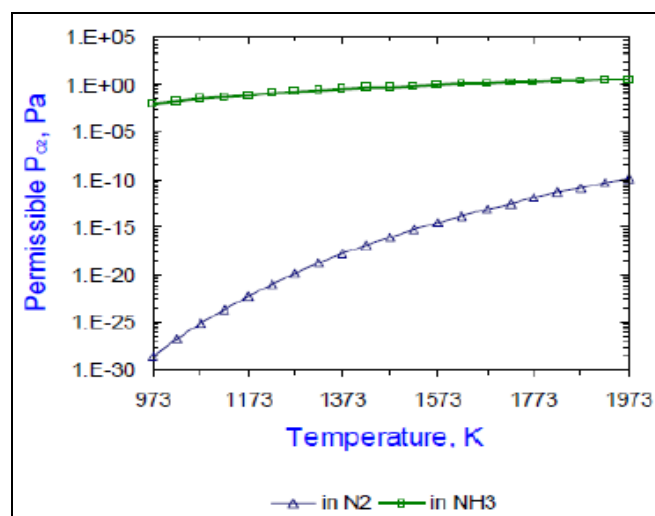


Figure 20: Permissible oxygen partial pressure for nitrogen and ammonia vs. temperature [51]

## 4.2.1 The role of magnesium

The mechanism of nitride formation is not clear yet. If the reaction needs a “carrier” element to occur, it is called “indirect” or “substitution reaction”. Dyzia et al. [57] demonstrated that aluminum nitrides are the result of an indirect synthesis. The addition of magnesium to the melt promotes  $Mg_3N_2$ , which acts as vehicle for the precipitation of AlN according to the reaction:



Hon et al. [59] concluded that the low activation energy of ammonia makes the direct mechanism not feasible and its kinetics unfavorable, causing incomplete nitrogen reaction and segregation on the top of the melt. Therefore, the indirect method, based on Mg to catalyze the reaction, is more favorable for aluminum nitrides formation. On the other side, Huashun et al. [60] affirmed that the possibility for  $Mg_3N_2$  particles to precipitate in the melt is very low, since an AlN film on the top of the melt hinders this formation. The present study support the theory of the direct reaction, where the AlN particles are synthesized from the reaction of ammonia with the melt at the bubble surface and detach from the bubble itself when it reaches the top surface of the melt. This can lead to segregation in the upper part of the crucible.

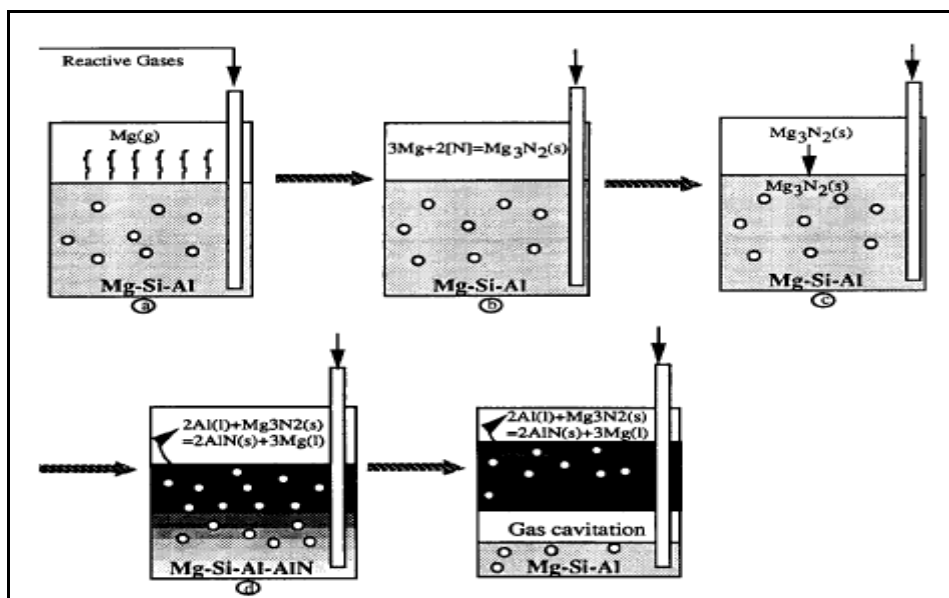


**Figure 21: Mechanism of indirect nitridation [59]**

Zheng and Reddy [58] observed that despite Mg could act as an oxygen getter, the addition of small quantity in aluminum doesn't significantly improve the formation of AlN. The hypothesis is that the bubble residence time was too short to allow magnesium to exert the action of oxygen

getter. When ammonia is bubbled, nitridation of magnesium is enhanced by the presence of hydrogen, which contributes to lower the oxygen content in the melt. Tyagi et al. [58] calculated the Gibbs energy change for nitridation of Mg- 30 wt.% Al with nitrogen as the gaseous precursor. From the thermodynamic analysis, reaction 4.4 is more stable than 4.3, thus more likely to occur. Despite this consideration, almost no nitrides have been found. When ammonia is bubbled, 14 wt.% of AlN can be detected. Therefore, what stated for aluminum applies for magnesium melts too.

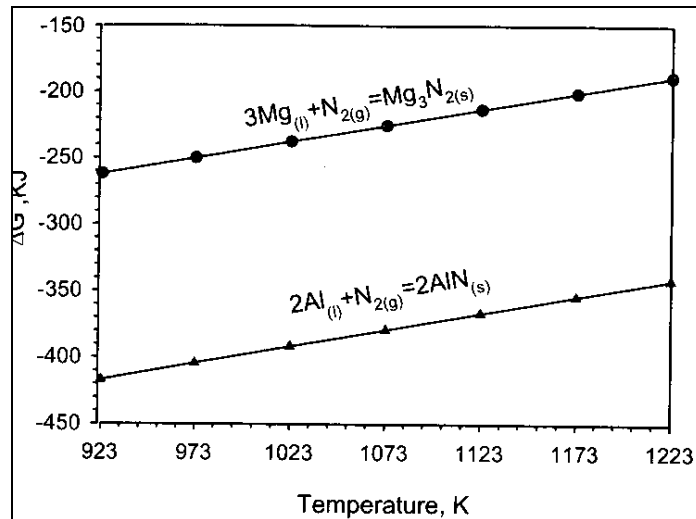
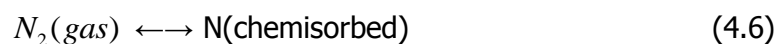


Figure 22: Gibbs energy change for nitridation of aluminum and magnesium [59]

### 4.3 Kinetics of the gas-liquid process

In order to react with the melt, the nitrogen has to diffuse from inside the gas bubble to the liquid aluminum. The two-film model - Figure 23 - has been adopted to explain the diffusion-reaction process to form the reinforcement phase [51,52]. Five steps are involved when ammonia gas is bubbled. It is necessary to identify which one acts as the rate-controlling step for the synthesis of the nitrides.

- Step 1: dissociation of ammonia into hydrogen and nitrogen molecules
- Step 2: mass transfer of  $N_2$  molecules from the gas bulk to the gas-liquid interface
- Step 3: chemisorption of  $N_2$  molecules at the gas-liquid interface:



- Step 4: mass transfer of nitrogen atoms in the liquid boundary layer:

$$N(xN,i) \rightarrow N(xN,o) \quad (4.7)$$

- Step 5: growth of solid AlN particles in the liquid boundary layer and in the liquid bulk according to Equation 4.3.

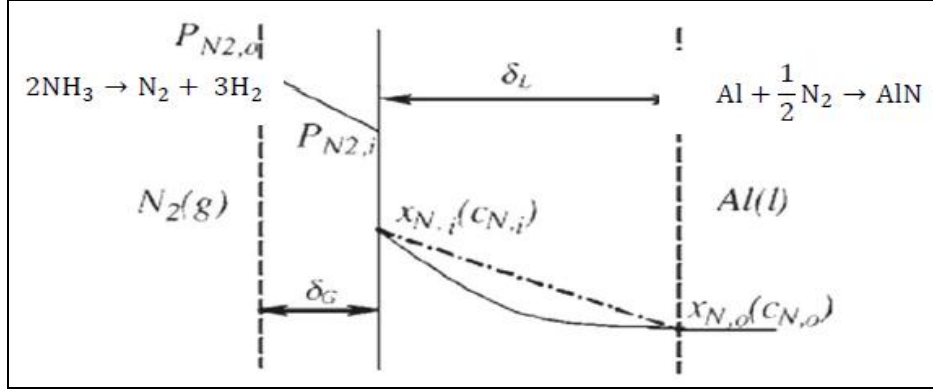


**Figure 23: Two-film model describing the mechanism of the Al melt-N<sub>2</sub> gas reaction [53].**

Reddy et al. [51-54] noticed that when nitrogen is used as the precursor gas, the rate-limiting step is the chemisorption of nitrogen molecules at the interface (Step 3). In the case of ammonia gas, the rate-limiting step is the diffusion of nitrogen atoms in the liquid boundary layer (Step 4), since the presence of hydrogen accelerates step 3 by reacting with the oxygen deposited on the gas-liquid interface. Despite this, the presence of oxygen due experimental conditions, can be lowered by ammonia only to a certain extent. Sometimes, the rate-limiting step of the reaction is more likely to be the chemisorption of nitrogen atoms on the gas-liquid interface. Equation 4.6 consists of three sub-steps:

1. Nitrogen molecules must be dissociated into nitrogen atoms
2. Nitrogen atoms must be chemisorbed from the gas-liquid interface
3. Nitrogen atoms must then be desorbed by the gas-liquid interface to diffuse in the liquid metal.

The rate of nitrogen molecules chemisorptions at the gas-liquid interface is:

$$r_{N,a} = c(2\pi MRT)^{-\frac{1}{2}} \left( P_{N_2,i} - \frac{x_{N,i}}{K_{(12)}} \right) \exp\left(\frac{-E_a}{RT}\right) \quad (4.8)$$

where  $c$  is a constant,  $M$  is the molar mass of the gas molecule,  $R$  the gas constant,  $T$  the temperature,  $E_a$  the activation energy for chemisorption of the gas at the interface,  $P_{N_2,i}$  and  $x_{N,i}$  the pressure of  $N_2$  gas and the concentration of chemisorbed nitrogen atoms at the interface

respectively and  $K_{(12)}$  the equilibrium coefficient of reaction 4.6. The activation energy is very high (308 kJ / mol), which renders the rate of nitrogen chemisorptions very slow. The nitrogen molecules can be chemisorbed only if their energy overcomes the activation energy, while the chemisorption of oxygen molecules is much more favorable, since it consistently lowers the Gibbs free energy of the system -Figure 24-. Another factor that lowers the rate of chemisorptions of nitrogen molecules the gas-bubble coverage -Figure 25-: the nitrogen molecules in the gas bulk might be unevenly distributed and thus cluster in certain spots, so that their chemisorptions would not be homogenous on the gas-liquid interface. As a result, the mass transfer of nitrogen atoms in the bulk liquid would be affected.

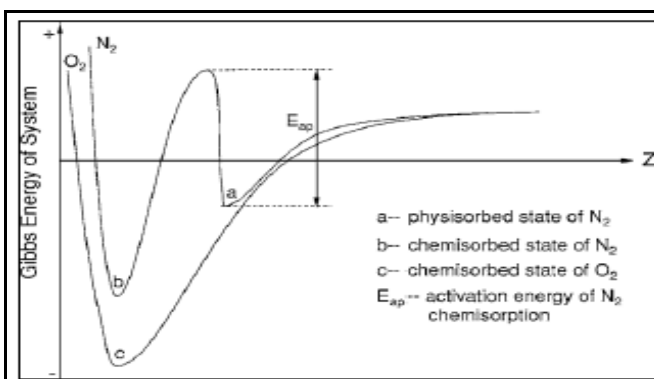


**Figure 24: Diagram of energy change of the system caused by chemisorption of N2-O2 pair [53]**

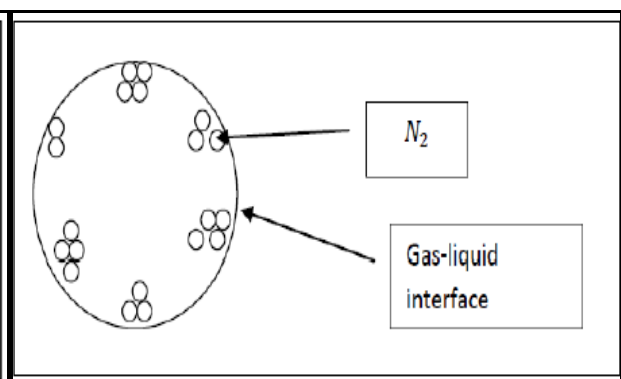


**Figure 25: Gas-liquid interface uneven covered from nitrogen molecules**

## 5. Concluding remarks

Nanocomposite materials offer improved performance when compared to monolithic alloys and microcomposites. The possible applications of these materials are numerous and involve several market fields. Multi-functional materials with novel properties have been engineered. Although, the size reduction to the nano-meter scale poses new technologic challenges that will have to be overcome, such as particle agglomeration and de-bonding from the matrix. The research is currently assessing manufacturing processes and characterization techniques for these materials. The role of atomic-scale forces (Van der Waals attraction and electrostatic repulsion) must be also taken into account to fully understand the mechanics of particles interaction. Most of conventional fabrication processes are unable to solve these issues or are industrially non-feasible. In-situ techniques have been found to provide a homogeneous dispersion and limited costs, though their effectiveness on an industrial scale hasn't been confirmed yet. The synthesis of aluminum nanocomposites via gas injection in a reactive melt belongs to this category. The range of matrix materials that can be employed is broad and the reinforcement can be tailored through the choice

of the precursor gas. The process is flexible and inexpensive. On the other side, very high temperatures (around 1300 K) are needed to catalyze the reaction. The kinetics of particle formation is not clear yet. The reaction rate is controlled by many factor and is strongly dependent from the injected gas and from alloying elements such as magnesium. Further investigation is required for a deep understanding of process dynamics. Once this target has been achieved, the scalability of the method can be pursued.

## *References*

1. S.Rawal: "Metal Matrix Composites for Space Applications", Journals of Materials 53, 4, 2001, pp.14-17.
2. www. Secat.net, Aluminum Association, "Aluminum Matrix Composites Materials of the Present or of the Future?", 2002.
3. www.almmc.com: "Discontinuously Reinforced Al has come to an edge".
4. P.E.C. Camargo, K. G. Satyanarayama, F. Wypych, "Nanocomposites: Synthesis, Structure, Properties and Opportunities", Material Research 12, 1, 2009, pp. 1-39.
5. S. Choi, H. Awaji, "Nanocomposites: a new material design concept", Science and Technology of Advanced Materials 6, 2005, pp. 2-19.
6. S. M. Zebarjad, S. A. Sajjadi, E. Z. Vahid Karimi, Influence of nanosized Silicon Carbide on Dimensional stability of Al/SiC Nanocomposite, Research Letter in Material Science, Vol.2008, Article ID 835746
7. Z.Ren and S.Chen, Mechanical properties of nanometric particulates reinforced aluminum composites, <http://www.materials.unsw.edu.au/NanoWeb>.
8. L.Fischer, Literature Survey Report: Nano-Dispersion Strengthening of Aluminum, Introduction to research, 2004, University of Colorado .
9. Unknown Author, "Microstructures and Mechanical Strengthening Mechanisms of Nanoparticle reinforced Mg-based composites".
10. Cecilia Borgonovo, "Chapter II, Literature review", Aluminum Nanocomposite Materials for High Temperature Application, University of Bologna, 2009.
11. Zhang and Chen, "Consideration of Orowan strengthening effect in particulate-reinforced metal matrix nanocomposites: A model for predicting their yield strength", Scripta Materialia 54, 2006, pp. 1321–1326.
12. M. Cournil, F.Gruy, P. Cugnet, P. Gardina, H. Saint-Raymond, "Model of aggregation of solid particles in nonwetting liquid medium", Centre SPIN, URA CNRS 2021, Ecole Nationale Supérieure des Mines de Saint-Etienne
13. "Particle collision and aggregation", Oceanography 54--Marine Geological Processes-- Autumn Quarter 2002.
14. G cao, J. kobliska, H. Konishi, and X. li, "Tensile Properties and Microstructure of SiC Nanoparticle–Reinforced Mg-4Zn Alloy Fabricated by Ultrasonic Cavitation–Based Solidification Processing", Metallurgical and Material Transaction, 39A, 2008

15. S. Melis, A. Sorti, "Effect of Fluid Motion on the Aggregation of Small Particles Subject to Interaction Forces", *AIChE Journal*, 45, 7, 2009.
16. Rhonda Lee-Desautels, "Theory of van der Waals Forces as Applied to Particulate Materials", *Educ. Reso. for Part. Techn.* 051Q-Lee
17. W. Zhou, Z. M. Xu, "Casting of SiC Reinforced Metal Matrix Composites", *Journal of Materials Processing Technology* Vol. 63, 1997, pp. 358-363 . 7
18. Fei, Katgerman, Kool, "Production of SiC particulate reinforced aluminium composites by melt spinning, *Journal of material science*", 1994, pp.6439-6444 . 27
19. Suresh, Mortensen, Needleman, "Fundamentals of metal matrix composites", Butterworth-Heinemann ed., 1993
20. A. Evans, C. San Marchi, A. Mortensen, "Metal Matrix Composites in Industry: An Introduction and a Survey", Springer, 2003
21. P. M. Ajayan, L. S. Schadler, P. V. Braun, "Nanocomposite science and technology", Wiley-VCH, 2003
22. C. C. Koch, "Nanostructured materials: processing, properties, and applications", William Andrew, 2006
23. Krishan Kumar Chawla, "Metal matrix composites", Birkhäuser, 2006
24. Z.Y. Ma, Y.L. Lia, Y. Liang, L F. Zheng , J. BP, S.C. Tjong, "Nanometric Si<sub>3</sub>N<sub>4</sub> particulate-reinforced aluminum composite", *Materials Science and Engineering A219*, 1996, pp. 229-231
25. Peng et al., "Manufacturing method for aluminum matrix nanocomposites", United States Patent, 7297310
26. Claudio L. De Castro, Brian S. Mitchell, "Nanoparticles from Mechanical Attrition", *Synthesis, Functionalization and Surface Treatment of Nanoparticles*, 2002.
27. C. C. Koch, "Nanostructured materials: processing, properties, and applications", William Andrew, 2006
28. D.L. Zhang, J. Liang, J. Wu, "Processing Ti<sub>3</sub>Al-SiC nanocomposites using high energy mechanical milling", *Materials Science and Engineering A* 375-377 , 2004, pp. 911-916
29. Guozhong Cao, "Nanostructures & nanomaterials: synthesis, properties & applications", Imperial College Press, 2004
30. Y. Yang, X. Li, Ultrasonic Cavitation Based Nanomanufacturing of Bulk Aluminum Matrix Nanocomposites, *Journal of Manufacturing Science and Engineering*, Vol.129,(2007), pp.497-501
31. Y. Yang, J. Lan, X. Li, Study on bulk aluminum matrix nano-composite fabricated by ultrasonic dispersion of nano-sized SiC particles in molten aluminum alloy, *Material Science and Engineering A380* (2004), pp. 378-383.

32. Y. Yang, X. Li, X. Cheng, Ultrasonic-assisted fabrication of metal matrix nanocomposites, *Journal of material science*, Vol.39 (2004), pp.3211-3212
33. R. Ashtana, "Solidification Processing of Reinforced Metals", Trans. Tech Publications, 1997
34. G. Kaptay, "Interfacial criteria for producing ceramic reinforced metal-matrix composites", *Proc. Int. Conf. High Temperature Capillarity* 29 June-2 July 1997, Poland
35. Gierlotka, Synthesis of Metal-Ceramic Nanocomposites by high pressure infiltration, *Science24.com*
36. Zheng, Wu, Reddy, "In-Situ Processing of Al Alloy Composites", *Advanced Engineering Materials* 5, No. 3, pp. 167-173, 2003
37. D. Apelian, "Processing Challenges of Light Weight, Light Specific Strength Metallic Materials".
38. S.C. Tjong, Z.Y. Ma, "Microstructural and mechanical characteristics of in situ metal matrix composites", *Material Science and Engineering* 29, Review Report, pp.49-113, 2000.
39. A.G. Merzhanov, "Self-Propagating High-Temperature Synthesis (SHS)", Institute of Structural Macrokinetics and Materials Science of the Russian Academy of Sciences
40. C.M. Ward-Close, Minor, Doorbar, "Intermetallic-matrix composites. A review", *Intermetallics* 4, pp.217-229, 1996.
41. Chu et al., "Metal Product Containing Dispersoid Form In-Situ", US Patent 6723282, April 2004
42. Z.Y. Chen, Y.Y. Chen, Q. Shu, G. Y. An, D. LI, and Y.Y. Liu, "Microstructure and Properties of In Situ Al/TiB<sub>2</sub> Composite Fabricated by In-Melt Reaction Method", *Metallurgical and material Transactions A* 31A, pp. 1959-1965
43. Koczak et al., "In situ process for producing composite containing refractory material", US Patent 4808372, February 1989
44. Nam P. Suh Sutek Corporation, "Mix alloy Process", US Patent 4278622 and 4279843, July 1981.
45. Nam P. Suh Sutek Corporation, "Mix alloy Process", US Patent 4706730 and 4890662 .
46. Bei, "A review of directionally solidified intermetallic composites for high-temperature structural applications", *Journal of materials science* 39, pp.3975 – 3984, 2004
47. M. Fleming, "Solidification Processing", Mc Graw-Hill, New York, 1974
48. J.M. Yang, " The mechanical behavior of in situ NiAl-refractory metal composites", *Journal of Materials Review*, 1997
49. Hirano, "Application of eutectic composites for 1700 °C-class gas turbine", Japanese National Project, 2007

50. Zhao et al., "Nickel-base sigma-gamma in-situ intermetallic matrix composite", US Patent 5858558.
51. Zheng and Reddy, "Kinetics of In-Situ Formation of AlN in Al Alloy Melts by Bubbling Ammonia Gas", Metallurgical and Material Transaction 34B, pp. 793-805, 2003.
52. Zheng, Wu, Reddy, "In-Situ Processing of Al Alloy Composites", Advanced Engineering Materials 5, No. 3, pp. 167-173, 2003.
53. Zheng, Reddy, "Mechanism of in-situ formation of AlN" in Al melt using nitrogen gas", Journal of Material Science 39, pp. 141-149, 2004.
54. Reddy et al. , "Production of Metal/Refractory Composites by Bubbling Gas Through a Melt" , US Patent 6343640, June 2002.
55. R.F. Shyu, F.T. Weng, C.T. Ho, "In-situ reacted titanium nitride-reinforced aluminum alloy composite", Journal of Materials Processing Technology 122, pp. 301–304, 2002.
56. Shyu and Ho, "In-situ reacted titanium carbide-reinforced aluminum alloys composite", Journal of Materials Processing Technology 171, pp. 411–416, 2006.
57. M.Dyzya, J.Sleziona, "Aluminum Matrix Composites Reinforced with AlN particles formed by in-situ reaction", Archives of Material Science and Engineering 31, pp.17-20, 2008
58. S.Tyagi, Q.Zheng and R. Reddy: "In-situ synthesis of AlN reinforced Magnesium Alloy Composites Using Gas Bubbling method", Aluminum 2004, TMS.
59. Hou, Mutharasan, Koczak, "Feasibility of aluminum nitride formation in aluminum alloys", Materials Science and Engineering A195, pp. 121-129, 1995.
60. Yu Huashun, J.D. Kim, S.B. Kang, "The formation of AlN and TiN particles during nitrogen bearing gas injection into Al–Mg–Ti melt", Materials Science and Engineering A 386, pp. 318–325, 2004.

### *Table of figures*

Figure 1: Global outlook of metal-matrix composites by application segment (2004-2013) .....	10
Figure 2: TEM image of nano-particles embedded in aluminum grains [5] .....	12
Figure 3: a) Loose and clustered particles. The interfacial area is reduced in the cluster; b) Clusters of SiC nano-particles [14].....	14
Figure 4: Forces acting between two particles [15].....	16
Figure 5: SiC nano-particles on A356 aluminum alloy fractured surface .....	17
Figure 6: EDS spectrum of a SiC nano-particle on the fractured surface .....	17
Figure 7: Manufacturing methods for metal-matrix nanocomposites.....	18

Figure 8 Powder processing, hot pressing, and extrusion process for particulate reinforced composites [23].....	20
Figure 9: Grain size and strain vs. milling time for WC particles [26].....	14
Figure 10: Schematic of ultrasonic solidification      Figure 11: Strength vs. nano-particles percentage [30,31].....	22
Figure 12: Schematic of spraying process [34] .....	23
Figure 13: Combustion synthesis process.....	25
Figure 14: XD process.....	26
Figure 15: DIMOX process.....	27
Figure 16: Microstructure of the directionally solidified Al <sub>2</sub> O <sub>3</sub> /YAG after 0 and 250 hours at 1700 C°[49] .....	29
Figure 17: Schematic of gas-liquid process [52] .....	25
Figure 18: AlN particles in Al matrix via gas-liquid .....	30
Figure 19: Dissociation temperature for methane gas and ammonia gas [52] .....	31
Figure 20: Permissible oxygen partial pressure for nitrogen and ammonia vs. temperature [51] .	32
Figure 21: Mechanism of indirect nitridation [59].....	33
Figure 22: Gibbs energy change for nitridation of aluminum and magnesium [59].....	34
Figure 23: Two-film model describing the mechanism of the Al melt-N <sub>2</sub> gas reaction [53]. .....	35
Figure 24: Diagram of energy change of the system .....	31
Figure 25: Gas-liquid interface uneven covered .....	36

**APPENDIX B**  
**In-situ Processing of Aluminum**  
**Based Nanocomposites: *Model***  
***and Experimental Validation***

# **In-situ Processing of Aluminum Based Nanocomposites:**

## *Model and Experimental Validation*

### **C. Borgonovo, D. Apelian**

---

### *Abstract*

Aluminum nitride (AlN) superior thermal and electrical properties are ideal for high-temperature applications as well as for packaging and optoelectronic purposes. Aluminum based composites reinforced with AlN have been manufactured via an in situ gas-assisted process, where a nitrogen-bearing gas is injected in the molten aluminum at 1273-1323 K. The feasibility of the process has been evaluated both by means of a simulation model and experimentally. The reliability of the model has been validated and the feasibility of the method proved. The process has to be carried out in an inert atmosphere in order to avoid the contamination of the melt by the oxygen. Addition of Mg has been found to be necessary, since it lowers the oxygen content in the melt by forming MgO and thus, favoring the nitridation reaction  $2Al + N_2 \rightarrow 2AlN$ . The size of the particles varies from 1- 3  $\mu\text{m}$  to sub-micron dimensions when the gas is injected for longer times. The dispersion of the reinforcement has also been improved for longer bubbling times. The addition of Si has been found to be detrimental for the synthesis of AlN.  $\text{Mg}_2\text{Si}$  phase precipitates, replacing the formation of MgO and hindering aluminum nitridation.

# *Contents*

1. Introduction
2. Model formulation
  - 2.1 Objectives and expected outcomes
    - 2.1.1 Verify the feasibility of the process
    - 2.1.2 Predict amount and distribution of the secondary phase
  - 2.2 Mathematical background
    - 2.2.1 Assumptions
    - 2.2.2 Governing equations
    - 2.2.3 Total gas-liquid interface area ( $A_t$ )
    - 2.2.4 Rate of formation of AlN particles ( $\theta_{\text{AlN}}$ )
  - 2.3 Modeling tools
    - 2.3.1 Calculation domains
    - 2.3.2 Meshing and boundary conditions
    - 2.3.3 Sub-domain settings
  - 2.4 Results
3. Experimental verification
  - 3.1 Description of experiments
    - 3.1.1 Experimental set-up
    - 3.1.2 Sample preparation and analysis
    - 3.1.3 Matrix of experiments
  - 3.2 Results and discussion
    - 3.2.1 Microstructure analysis
    - 3.2.2 Model verification

## 4. Conclusions

*List of symbols*

*References*

*Table of figures*

## 1. Introduction

Aluminum based nanocomposites have increasingly gained attention as weight-saving functional materials with improved mechanical properties that can't generally be achieved by monolithic alloys. Carbide or nitride particles are added to aluminum matrix to confer superior hardness, wear resistance and dimensional stability at high temperatures. Several manufacturing methods such as mechanical stirring, infiltration and powder metallurgy –see Appendix A- have been employed so far. None of these conventional processes has been able to provide a homogeneous distribution of the secondary phase in the metal while being cost effective and easy to scale. On the contrary, in-situ synthesis routes have been found to be innovative and advantageous in the fabrication of high-performance composite materials [1,3,6]. The secondary phase is created inside the metal itself through a chemical reaction that can occur at solid, liquid or gaseous state. The in-situ creation of the reinforcement ensures clean and thermodynamic stable interfaces, good particle dispersion and cost effectiveness. Moreover, it is possible to produce composites with a broad variety of matrix materials (aluminum, titanium, copper, nickel and iron) and reinforcing particles (borides, carbides, nitrides, oxides and their mixtures). Application fields range from the automotive market to aerospace applications. Among the wide range of in-situ techniques, the synthesis of nitride particles by means of a gas-assisted reaction has shown promising features. Hou et al. [2] have been able to manufacture aluminum matrix composites reinforced with AlN with a diameter smaller than 0.1  $\mu\text{m}$ . Zheng et al. [3] have converted 14% weight of Mg-Al alloy into aluminum nitrides. The process involves the introduction of a nitrogen-based gas in the melt for the nitridation of aluminum to occur. It is carried out in an inert atmosphere and can take from thirty minutes up to several (9-10) hours. Control of process variables such as matrix and gas composition, as well as processing time, allows to tailor amount and size of the reinforcement [3,4].

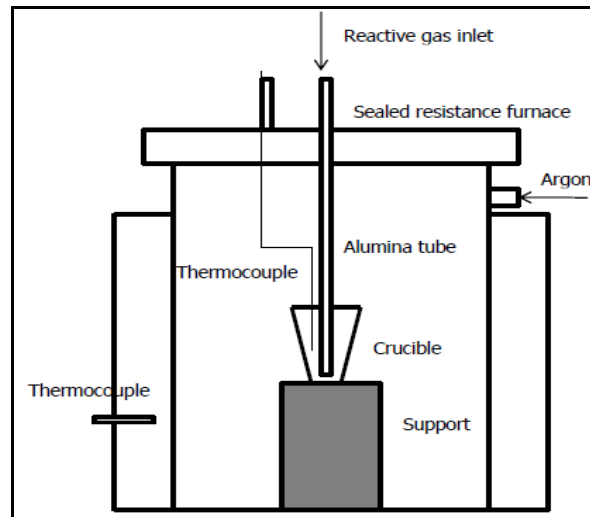


**Figure 1 : Schematic of in-situ gas/liquid process**

Aluminum nitride is a refractory compound characterized by attractive properties such as high thermal conductivity, high electrical resistance, low dielectric constant, and a thermal expansion coefficient matching silicon [5]. It is suitable for producing substrates and packaging materials in high-power integrated circuits, as well as coatings, insulators and optoelectronic devices. An epitaxially grown thin film of AlN on silicon wafers is also used for surface acoustic wave sensors (SAW) for its exceptional piezoelectric properties. Although liquid nitridation has been widely investigated over the years, the dynamics of AlN formation isn't clear yet. Two different formation mechanisms have been identified for aluminum alloys: direct nitridation according to the reaction  $2Al + N_2 \rightarrow 2AlN$  and indirect nitridation assisted by a catalyst such as magnesium. The latter involves the formation of an intermediate phase ( $Mg_3N_2$ ) through the reaction  $3Mg + N_2 \rightarrow Mg_3N_2$  followed by the substitution reaction  $Mg_3N_2 + 2Al \rightarrow 2AlN + 3Mg$ . Several publications refer to this mechanism as more likely to be responsible for nitrides formation than direct nitridation [7,8,10]. Shtapitanonda and Margrave [9] in 1956 observed the tendency of magnesium nitrides to form in the gaseous phase after the volatilization of magnesium in furnaces with a controlled atmosphere. The substitution reaction consequently occurs once the  $Mg_3N_2$  phase falls into the molten metal. Pech-Canul et al. [10] pointed out how the formation of magnesium nitrides is kinetically more favored than formation of AlN. Moreover, they confirmed the occurrence of the substitution reaction to form AlN, which is a more thermally stable compound at around the process temperature range (1273-1373 K). Despite this, no agreement about the formation mechanism (direct or indirect) has been achieved by the research.

The influence of dopants (Mg, Si) and oxygen content in the reactive gas has been found to be of great importance for the feasibility of the process, as well as the composition of the reactive gas.

Scholz and Greil [11] stated that with increasing Mg/Si ratio and decreasing oxygen content in the nitriding gas the conversion from Al to AlN is more favorable. Jinxiang et al. [12] investigated the influence of Mg and Si on the rate of nitride formation, underlining the predominant role of magnesium over silicon. Zheng and Reddy et al. [6] found that a higher amount of nitrides are formed when instead of nitrogen ammonia is used as reactive gas. Its oxygen-getter action, due to the dissociation of nitrogen and hydrogen at around 1273 K, results in a lower oxygen content and thus, a lower partial pressure inside the melt. The detrimental effect of oxygen is clear when the thermodynamics of the system is analyzed. The Ellingham diagram of the reaction through which aluminum oxides are formed  $4Al + 3O_2 \rightarrow 2Al_2O_3$  shows a lower Gibbs free energy when compared to the Gibbs energy of the nitridation reaction – see Figure 2a.

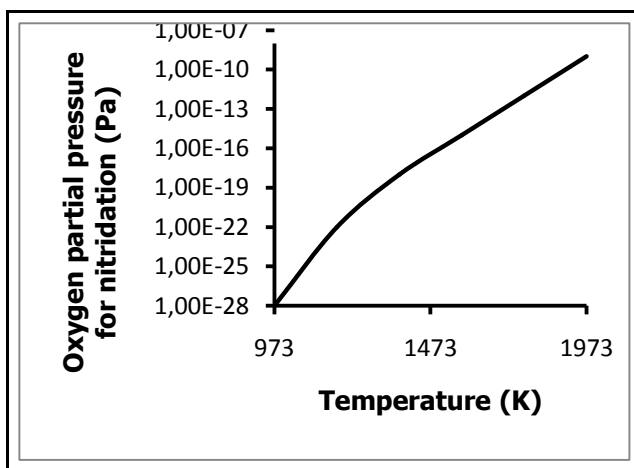


**Figure 2: a) Ellingham diagram for the nitridation and oxidation of aluminum [19]; b) Oxygen partial pressure for nitridation vs. temperature.**

Studies of the initial nitridation period of aluminum at 400 C° and higher show that the rate of nitridation is much slower than the rate of oxidation at a given temperature [12].

The influence of process temperature has also been investigated. Figure 2b shows the increase of the permissible partial pressure of oxygen necessary for the nitridation reaction. Moreover, the rate of formation of the reinforcement follows an Arrhenius-type equation with respect to temperature, increasing exponentially with it [9] The amount of secondary phase has also been noticed to be enhanced by increasing gas flow rates, bubbling times and decreasing nozzle diameter of the injection tube [6]. Process feasibility is not only dictated by the kinetics of the nitridation reaction. The dynamics of the bubbly flow rising in the melt at low Reynolds numbers (steady flow) affects the diffusion of nitrogen in the aluminum. During its motion in the liquid metal, the gas bubble is subjected to mass diffusion of nitrogen atoms towards the outside and change of hydrostatic pressure as it changes its position during the rise. These two factors cause the bubble diameter to change and therefore, its speed to be different along the crucible height.

The bubble might be rising too fast to allow the nitrogen atoms to diffuse ahead of the bubble surface and to react with the liquid. The time required for the nitrogen atoms to diffuse ahead of the gas interface is called *local diffusion time*. This time has to be smaller than the time required by the nitridation reaction to occur (*reaction time*), which has been found [12] to be around 10-7 seconds at 1273 K. If this condition is verified, the reinforcement could be synthesized. Process variables such as gas flow rate; atmospheric pressure and liquid viscosity can be modified to tailor the local diffusion time.

In this work, a model predicting the amount of reinforcement phase synthesized is presented. The size and velocity of the gas bubble are calculated and their impact on feasibility analyzed. Experimental verification of the model will also be pursued. In case the model is confirmed by experimental results, important considerations concerning the nitrides formation mechanism can be drawn. The effect of Mg and Si on process feasibility will also be investigated and a path to incorporate the alloy composition into the fluid dynamic model will be purposed.

## 2. Model formulation

### 2.1 Objectives and expected outcomes

The aims of the model are the following:

- Verify the feasibility of the process;
- Predict amount and distribution of the secondary phase.

#### 2.1.1 *Verify the feasibility of the process*

Feasibility can be mathematically expressed through Equation 1:

$$W_{AIN} = \int_0^t A_t \theta_{AIN} dt > 0 \quad (1)$$

where  $W_{AIN}$  indicates the total amount of AlN formed during the process.  $t$  is the bubble residence time,  $A_t$  the total gas-liquid interface and  $\theta_{AIN}$  the rate of formation of AlN particles. The model will be focused to determine  $A_t$  and  $\theta_{AIN}$  so that  $W_{AIN}$  can be quantified. Specifically, it will calculate the bubble diameter during the rise of the bubble in the melt. The bubble diameter  $d_b$  contributes to define  $A_t$  and  $\theta_{AIN}$  according to Equation 2, 3 and 4:

$$A_t = N_b A_b = N_b \pi \left( \frac{d_b}{2} \right)^2 \quad (2)$$

where  $N_b$  is the number of gas bubbles in the melt and  $A_t$  the bubble area.

$$\theta_{AIN} = EK_L(C^* - C_i) \quad (3)$$

where  $E$  is the enhancement factor (which accounts for the contribution of the nitridation reaction on the nitrogen concentration in the bulk –see 2.2.4-),  $K_L$  the mass transfer coefficient,  $C^*$  the nitrogen concentration at the gas-liquid interface and  $C_i$  the initial nitrogen concentration in the melt.

### 2.1.2 Predict amount and distribution of the secondary phase

Previous works [6] considered  $A_t$  and  $\theta_{AIN}$  as constant along the liquid domain (the crucible). As a consequence, the amount of reinforcement  $W_{AIN}$  formed at the bottom of the crucible results to be the same that at the top of it. Contrarily, the bubble diameter varies along the metal pool and as a consequence,  $A_t$  and  $\theta_{AIN}$  also vary. The amount of secondary phase synthesized will therefore change with the depth of the crucible (z-axis distribution). Nitrogen gas bubbles are subjected to mass transfer towards the bulk metal and to the decrease of hydrostatic pressure as they rise in the melt. The former causes the bubble to shrink whereas the latter to expand. These two phenomena are taken into account into the model in order to calculate the instantaneous diameter of the bubble as it rises. The profile of the nitrogen concentration from the center (where the injection tube is placed) of the crucible towards the periphery will also be simulated (x-axis distribution).

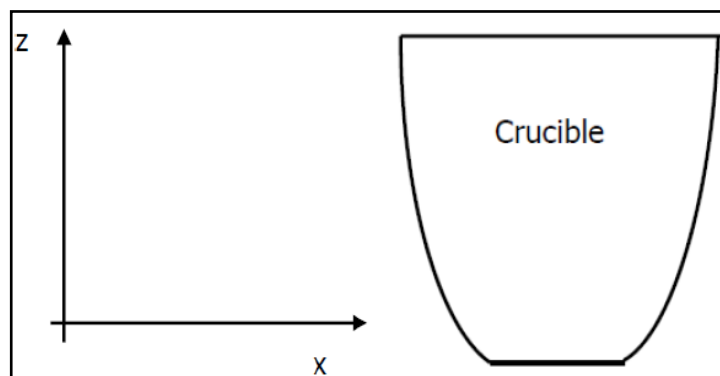


**Figure 3: Z-axis and x-axis distribution**

## 2.2 Mathematical background

In the present section model assumptions, governing equations and terms of Equation 1,2 and 3 are analyzed.

### 2.2.1 Assumptions

1. The bubble is spherical;
2. Diffusion and bubble shrink/growth occur isothermally;
3. Finite and steady liquid domain;
4. The liquid is incompressible;
5. Bubbles don't interact with one another;
6. The gas in the bubble is pure and obeys ideal gas law;
7. The bubble surface is contaminant-free
8. Henry's law applies at the gas-liquid interface to couple the gas pressure in the bubble with the dissolved gas concentration at the bubble surface;
9. Liquid phase resistance controls mass transfer in the melt;
10. Mass transfer in the liquid phase is ruled by Higbie's penetration theory;
11. Initial concentration  $C_i$  of nitrogen in the liquid bulk is zero;
12. Effects of the confining walls of the crucible on the bubbles are neglected.
13. The influence of melt composition (addition of alloying elements) on the nitridation reaction is not taken into account.

### 2.2.2 Governing equations

Navier-Stoke simplified expression for the problem of a bubble rising in the liquid whose size varies with time is the following:

$$\frac{dr_b}{dt} = \frac{(P_g - P_l)}{4\eta} - \frac{\gamma}{2\eta} \quad (4)$$

Where  $P_g$  is the pressure in the bubble,  $P_l$  the liquid pressure,  $\gamma$  the surface tension of aluminum and  $\nu$  the dynamic viscosity of the liquid.

Pressure and concentration at the bubble surface are coupled through Henry's law –Equation 6- and mass balance – Equation 7.

$$C^* = \frac{P_g}{He} \quad (5)$$

where  $He$  is Henry's constant.

$$\frac{d}{dt} \left( \frac{4\pi P_G r_b^3}{3RT} \right) = 4\pi r_b^2 D \left. \frac{\partial c}{\partial r} \right|_{r=r_b} \quad (6)$$

where  $R$  is the ideal gas constant,  $T$  the temperature and  $D$  is the diffusion coefficient of nitrogen in aluminum which depends from temperature according to the equation:

$$D = 3.75 \times 10^{-7} \exp\left(\frac{-3184}{T}\right) \quad (7)$$

The concentration gradient at the bubble surface  $\left. \frac{\partial c}{\partial r} \right|_{r=r_b}$  is determined by means of Fick's second law of diffusion in a steady liquid domain (the convection term is neglected):

$$\frac{\partial c}{\partial t} = D \frac{\partial^2 c}{\partial r^2} \quad (8)$$

The initial condition for the pressure in the gas bubble  $P_{GO}$  is given by the hydrostatic pressure at the nozzle of the injection tube, given by:

$$P_{GO} = P_{atm} + \rho_l gh + \frac{4\gamma}{d_{no}} \quad (9)$$

where  $P_{atm}$  is the atmospheric pressure,  $\rho_l$  the liquid density,  $h$  the crucible height and  $d_{no}$  the nozzle diameter of the injection tube. The initial condition for the concentration at the bubble surface is derived by Henry's law for  $P_G = P_{GO}$ , while in the liquid domain it's zero.

### 2.2.3 Total gas-liquid interface area ( $A_i$ )

Equation 2 defines the dependency of  $A_i$  from the bubble radius and the number of bubbles in the melt. The procedure to calculate  $N_b$  is the following:

$$N_b = \tau f_b = \frac{h}{U_b(r_b)} f_b \quad (10)$$

where  $\tau$  is the bubble residence time in the melt,  $U_b$  the bubble instantaneous rising velocity (function of bubble diameter) and  $f_b$  the frequency of formation of gas bubbles at the nozzle of the injection tube defined by:

$$f_b = \frac{V_g}{V_{bo}} \quad (11)$$

where  $V_g$  is the volume flux of the gas at the nozzle and  $V_{bo}$  the volume of the detaching bubble given by [13]

$$V_{bo} = \frac{4\pi}{3} \left(\frac{d_{bo}}{2}\right)^3 \quad (12)$$

$$d_{bo} = \left(\frac{6d_{no}\gamma}{g(\rho_l - \rho_g)}\right)^{1/3} \quad (13)$$

where  $d_{bo}$  is the diameter of the detaching bubble.  $V_g$  can be calculated through the ideal gas law approximation:

$$V_g = \frac{P_{in}T}{P_{GO}T_{in}} V_{in} \quad (14)$$

where  $P_{in}, T_{in}, V_{in}$  is the state of the gas at the inlet of the injection tube.

#### 2.2.4 Rate of formation of AIN particles ( $\theta_{AIN}$ )

##### *Mass transfer coefficient ( $K_L$ )*

The diffusion of nitrogen atoms in the liquid is ruled by Higbie's penetration theory [14,15], which considers the gas-liquid interface as composed of a variety of elements continuously brought up to the interface itself from the bulk of the liquid. The diffusion domain in the liquid –Figure 4- is a liquid boundary layer  $\delta$  given by:

$$\delta = \frac{\sqrt{D\pi t_d}}{2} \quad (15)$$

where  $t_d$  is the *local diffusion time* or *contact time*. It indicates how long the bubble stays in contact with a single element ahead of its interface and therefore, the time for the diffusion of nitrogen atoms in the liquid metal. Its expression has been formulated according to numerical simulations:

$$t_d = \frac{v}{U_b^2} \quad (16)$$

The mass transfer coefficient according to Higbie's theory is:

$$K_L = 2\sqrt{\frac{D}{\pi t_d}} \quad (17)$$

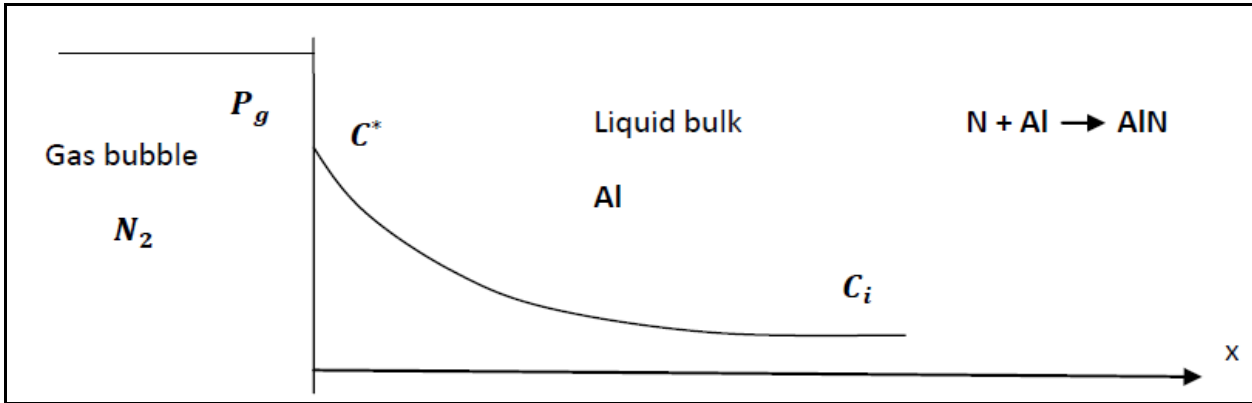


Figure 4: Schematic of the diffusion domain in the liquid (Higbie's penetration theory)

### Enhancement factor ( $E$ )

The synthesis of AlN lowers the content of nitrogen atoms in the melt after diffusion, increasing the nitrogen concentration gradient between the bubble surface and the melt. The Enhancement Factor is a non-dimensional index that accounts for such phenomenon. The nitridation reaction is a first order chemical reaction and it has been reported by Madhavi et al. in [16] as:

$$E = \frac{\sqrt{M' \left( E_i - \frac{E}{E_i} - 1 \right)}}{\tanh \sqrt{M' \left( E_i - \frac{E}{E_i} - 1 \right)}} \quad (18)$$

$$M' = \frac{\pi}{4} k_c C_{Al} t_d \quad (19)$$

$$E_i = \sqrt{\frac{D}{D_{Al}}} + \frac{C_{Al}^*}{C^*} \sqrt{\frac{D_{Al}}{D}} \quad (20)$$

where  $k_c$  is the kinetic constant of the nitridation reaction,  $D_{Al}$  the diffusion coefficient of aluminum and  $C_{Al}^*$  the aluminum concentration at the gas bubble surface.

### 2.3 Modeling tools

Different modules of COMSOL Multi-physics simulation software have been employed.

### 2.3.1 Calculation domains

For the calculation of the bubble radius a 1D linear domain has been adopted. It symbolizes the concentration boundary layer where the nitrogen atoms diffuse towards the liquid bulk. Since spherical symmetry applies, the calculation is carried out on the domain AB –Figure 5-. To simulate the distribution of the gas flow and the concentration of nitrogen atoms in the melt a 2D domain representing the injection tube in the crucible has been used – Figure 6.

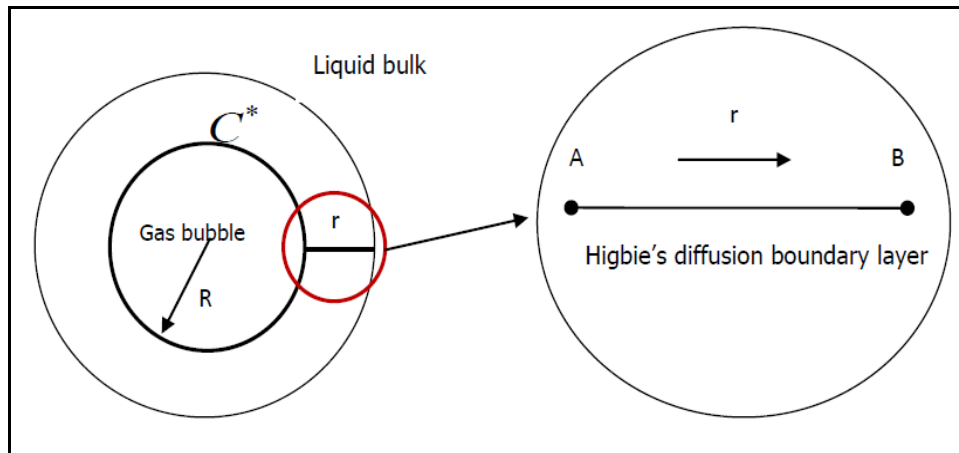


**Figure 5: Domain for the calculation of bubble radius**

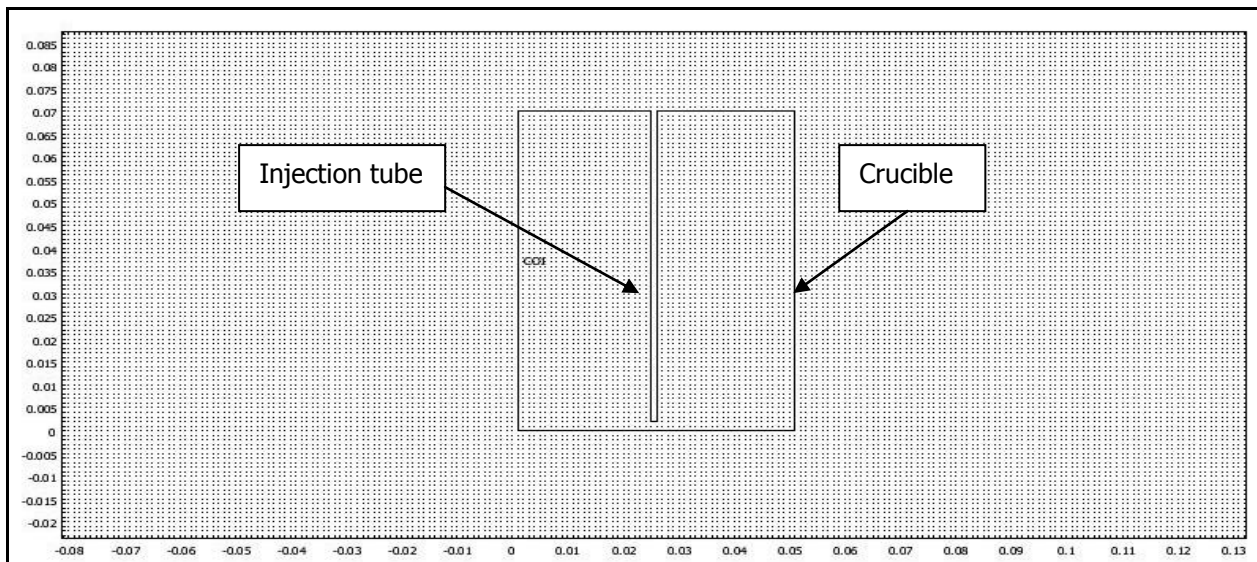


**Figure 6: Domain for the calculation of the distribution of the gas bubbles in the crucible**

### 2.3.2 Meshing and boundary conditions

#### Meshing

The 1D domain has been divided into linear elements 1.6e-6 m wide –Figure 7-. Two mesh modes have been employed for the 2D domain: a boundary layer at the boundaries and a free mesh on

the sub-domain –Figure 8-. A boundary layer mesh is a mesh with dense element distribution in the normal direction along specific boundaries. It is typically used for fluid flow problems to resolve the thin boundary layers along the no-slip boundaries where a layered quadrilateral mesh is employed. The mesher adjusts the number and the thickness of boundary in thin regions to avoid low quality elements and colliding boundary layers. The free mesh on the sub-domain consists of triangular elements with side 0.002 m wide that become more refined at the nozzle of the injection tube.

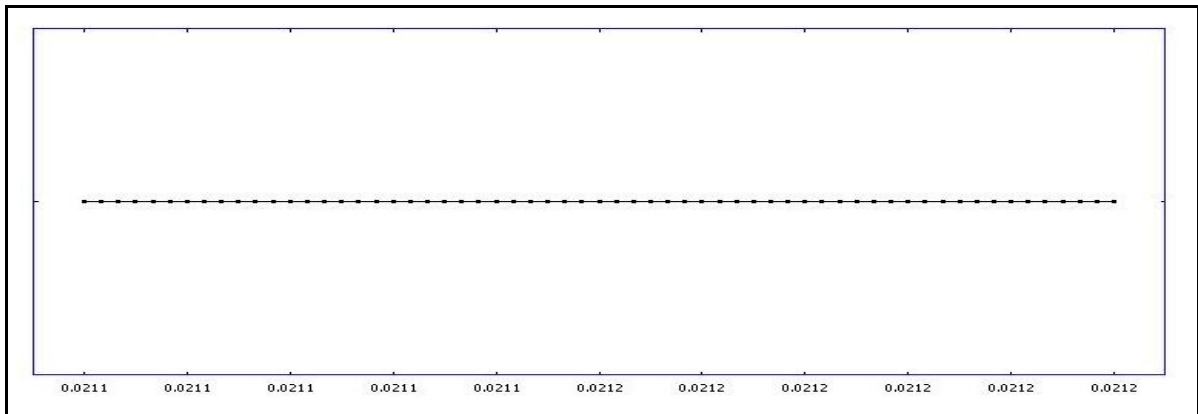


**Figure 7: Mesh of the 1D domain**

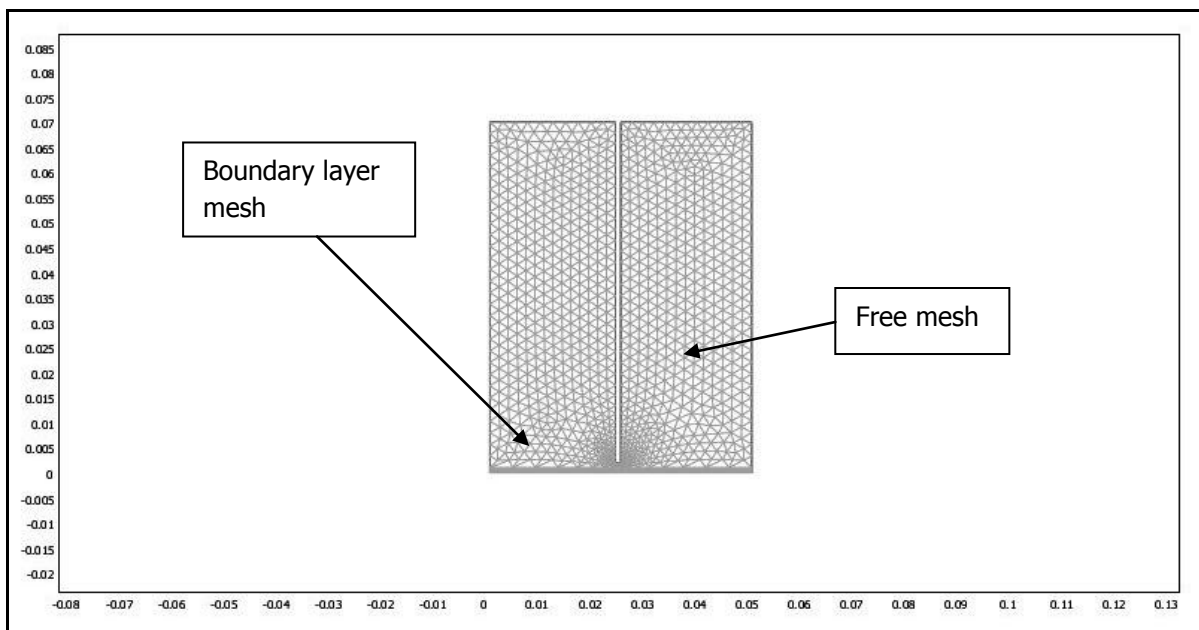


**Figure 8: Mesh of the 2D domain**

### *Boundary conditions*

Bubble radius is extreme A in Figure 5. Therefore, the calculation occurs on this boundary. The system of equations 4, 5 and 6 is solved for variables  $C^*$ ,  $P_G$ ,  $r_b$  using PDE Mode –Figure 9- of COMSOL Multiphysics. The Moving Mesh mode applied at the boundary A has been added to

visualize the change in bubble diameter with time. Equation 6 (Henry's law) is also the boundary condition for the Diffusion Mode that calculates the concentration profile on the linear sub-domain.  $C^*$ ,  $P_G$  are coupled through the Boundary Integration Variables Mode –Figure 10.

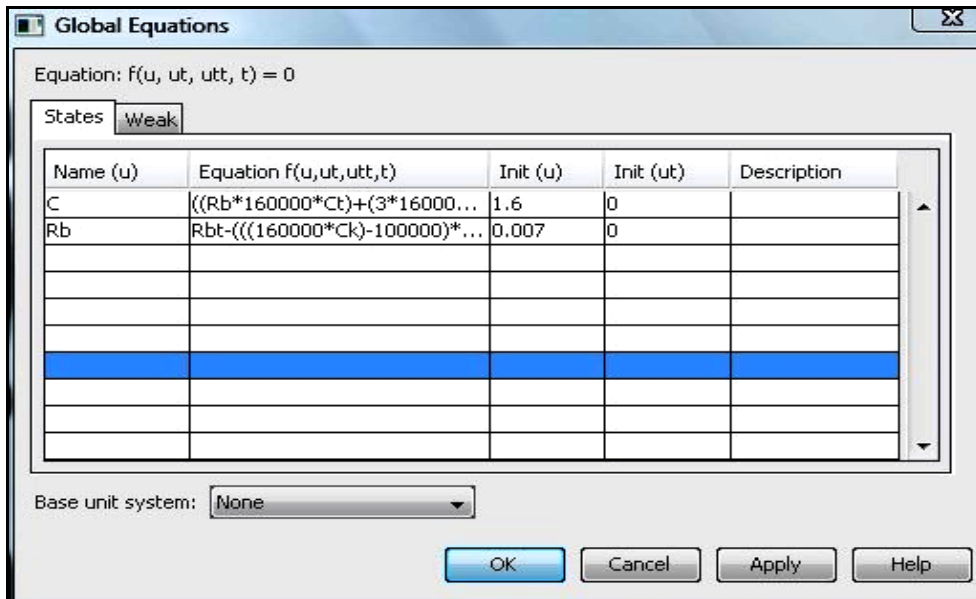


Figure 9: Global Equations Mode

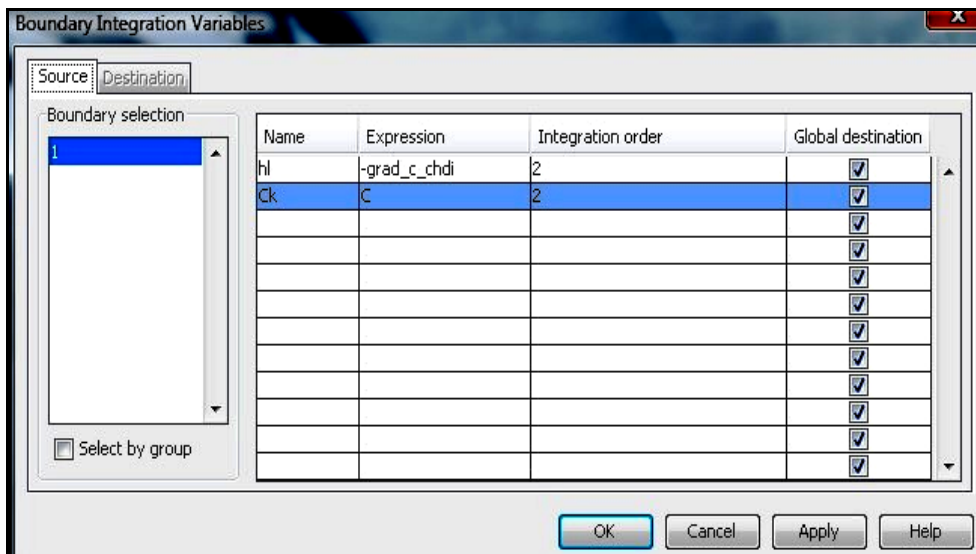
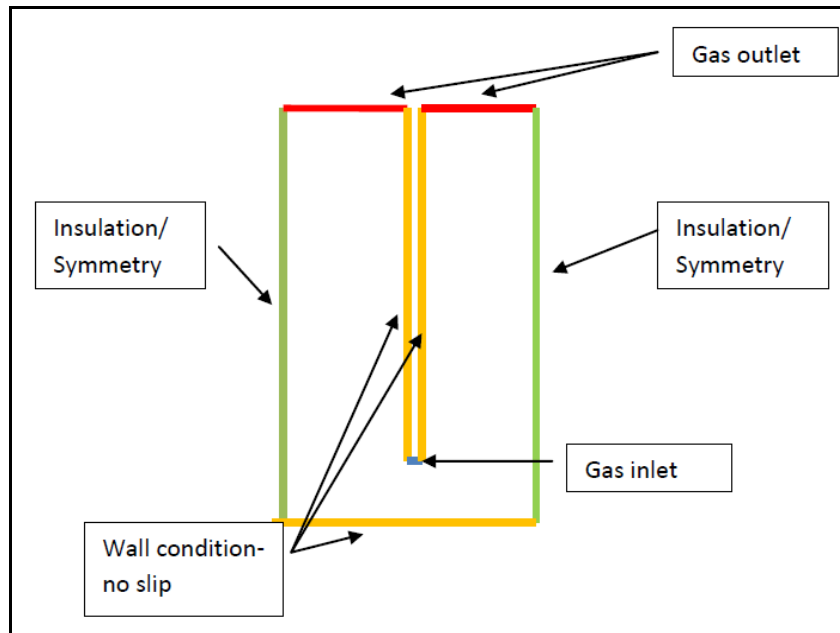


Figure 1026: Boundary Integration Variables Mode

A sketch of the boundary conditions employed in the 2D domain is reported in Figure 11.



**Figure 11: 2D domain boundary conditions**

### 2.3.3 Sub-domain settings

Table 1 summarizes the parameters of the model.

<i>Name</i>	<i>Value</i>
Liquid density ( $\rho_l$ )	$2377.23 - 0.331(T - 933) = 2255 \text{ Kg/m}^3$ [17]
Gas density ( $\rho_g$ )	$1.251 \text{ Kg/ m}^3$
Nozzle diameter ( $d_{no}$ )	$0.0015 \text{ m}$
Nozzle depth ( $h_{no}$ )	$0.0495 \text{ m}$
Nitrogen/aluminum surface tension ( $\gamma$ ) at 1273 K	$0.750 \text{ N/m}$ [18]
Dynamic viscosity of liquid ( $\eta$ )	$7.5 \times 10^{-4} \text{ (Pa s)}$
Molecular weight of molecular nitrogen (MWN)	$28e-3 \text{ (Kg/mol)}$
Molecular weight of aluminum (MWA)	$26.98e-3 \text{ (Kg/mol)}$
Henry's constant ( $He$ )	$163900 \text{ (Pa m}^3 \text{ /mol)}$
Diffusion coefficient of nitrogen in Al ( $D$ )	$3e-8 \text{ (m}^2\text{/s)}$

**Table 1: Model parameters**

For the calculation of the bubble diameter (1D domain) the Diffusion Mode –coupled with the concentration at the boundary through Henry's law- has been applied on the sub-domain. The

bubble distribution in the crucible (2D domain) has been simulated with the Bubbly Flow module on the sub-domain. It solves the Navier-Stokes equation for bubbly flows. The momentum equation for the gas-phase is solved in order to determine the gas velocity that will be employed according to Equation 16 and the turbulence in the liquid is solved based on the k-ε turbulence model –Figure 12. The turbulence contribution due to the interaction between the gas and the liquid phases is taken into account through a turbulent viscosity term. For the dissolution of the gas phase in the liquid the Convection-Diffusion application mode is added to model the concentration trend in the liquid. The two application modes are coupled through the mass transfer model included in the k-ε turbulence model, which provides the boundary condition for the Convection-Diffusion mode according to Henry’s Law –Equation 5.

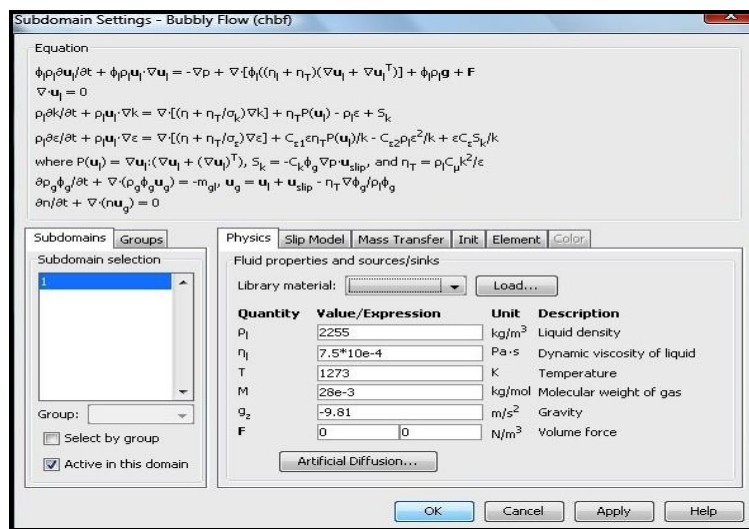


Figure 1227: Sub-domain settings of the Bubbly Flow Module

## 2.4 Results

Calculation of bubble radius is the first step to estimate the terms involved in the feasibility equation – Equation 1. It determines the total interface area  $A_i$  of the gas stream. The process variables adopted are reported in Table 2. They coincide with the variables used for the experimental validation.

Name	Value
Temperature ( $T$ )	1273 K
Gas flow rate ( $Q$ )	0.1 l/min
Gas injection time ( $t_b$ )	30 minutes, 1 h, 2h

Gas pressure at the tube inlet ( $P_{in}$ )	0.1 MPa
Gas temperature at the tube inlet ( $T_{in}$ )	295 K
Diameter of the detaching bubble ( $d_{bo}$ )	7 mm –Equation 14-
Initial pressure in the gas bubble ( $P_{GO}$ )	101095 Pa –Equation 10-

**Table 2: Model variables**

Figure 13 shows bubble radius as a function of the distance from the bottom of the crucible. In order to determine the real depth of the metal pool –the volume of aluminum decreases when it melts-, the same amount of matrix material used for the experimental validation has been melted in a crucible with the same dimensions of the one used for the experiments –Figure 16a- in a non-sealed furnace (induction furnace). In this way the melt can be observed by naked eye and the depth of the metal pool determined. It has been observed to be around 5 cm. It can be seen from Figure 13 that the metal is not deep enough to detect a considerable change in bubble radius. The contribution of hydrostatic pressure is almost negligible from bottom to top. However, the model can be adapted to any crucible depth. Gas velocity has been determined through the Bubbly Flow Mode. The values change only slightly along the crucible –always because of the small dimensions of the metal pool-. The average value of 0.6 m/s has been adopted. The contact time according to Equation 16 is  $9.238 \times 10^{-7}$  s. The order of magnitude ( $10^{-7}$ ) is the same of the time for the nitridation reaction to occur. This is the first requirement for the synthesis of AlN. The mass transfer coefficient has been calculated according to Equation 17 and found to be 0.22 m/s. The Enhancement factor according to Equation 18, 19 and 20 is averaged at 2. The concentration of nitrogen at the gas bubble interface has been calculated from the 1D model from the Diffusion Mode and since the scatter of the values in the crucible is small also in this case, it has been considered constant at  $0.62 \text{ mol/m}^3$ .

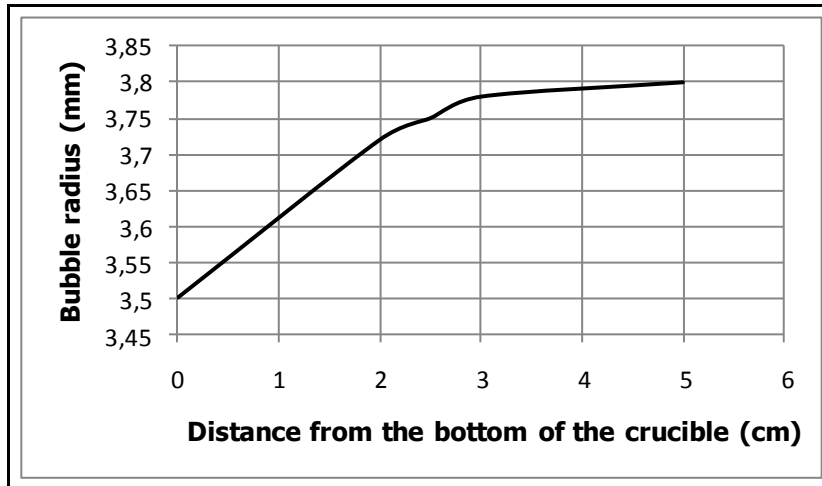


**Figure 13: Bubble radius vs. distance from the bottom of the crucible**

The frequency of bubble formation has been determined by Equation 11, 12 and 14 and found to be 78 bubbles per second. Such value has to be multiplied for the bubble residence time, which according to Equation 10 is 0.083 s.

Substituting all the values in Equation 1 we attain the moles per second of AlN formed:

$$W_{AlN} = \int_0^{t_b} 4.7 \times 10^{-5} dt \quad (21)$$

Expression 21 has been integrated on the three bubbling times and multiplied for the molecular weight of AlN -40.99 g/mol-. The results are reported in Table 3:

<i>Gas injection time (s)</i>	<i>AlN (g)</i>
30 minutes	2.05
1 h	6.78
2 h	13.33

**Table 3: Amount of AlN formed according to the model**

### 3. Experimental verification

Experiments have been pursued to verify the reliability of the model and thus, to confirm the feasibility of the process. In what follows the experimental setup and the matrix of experiments will be presented. The results will be presented and critically discussed in 3.2.

### 3.1 Description of experiments

#### 3.1.1 Experimental setup

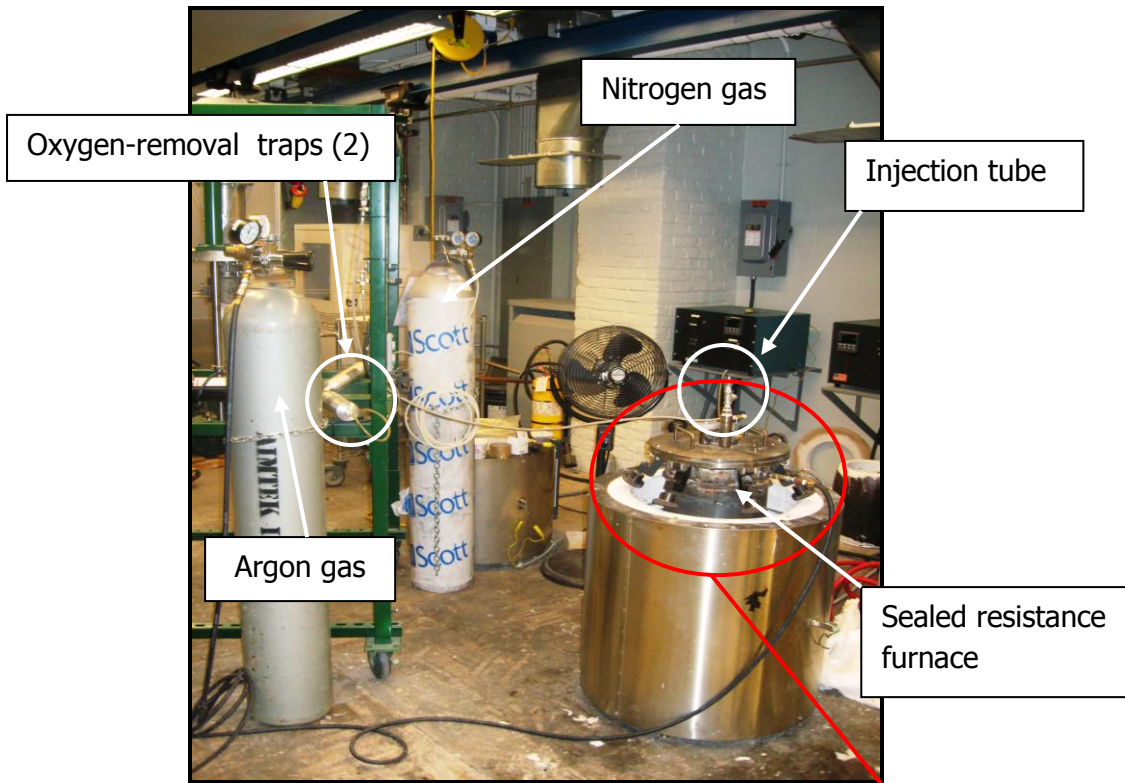
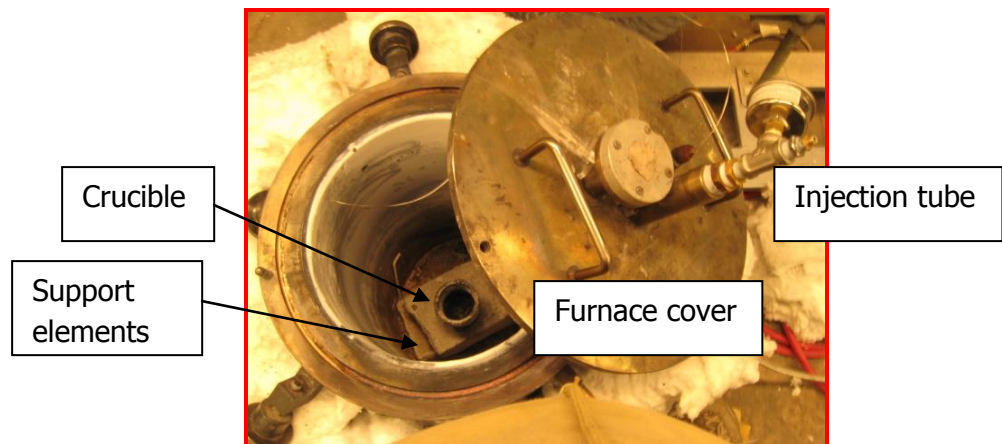


**Figure 1428: Experimental set-up**



Pure aluminum from ALCOA has been cut and cleaned together with the alloying elements -see Paragraph 3.1.2 for metal composition - in a BUEHLER ultrasonic cleaner for 20 minutes. Each experiment implies the melting of 150 g of metal in the sealed resistance furnace of Figure 14. The oxygen presence in the furnace must be avoided – see Paragraph 1. Thus, the casting must be carried on in a controlled atmosphere. The preparation of the furnace requires around two hours. The chamber must be cleaned in order to avoid the contamination of the melt by impurities (such

as dust) and after that sealing elements (silicone O-ring and plaster for the thermocouple fittings) are placed. A conic alumina crucible 7 cm high and with an upper diameter of 5 cm is positioned in the furnace with the help of a fiberscope video camera. The camera is inserted from the side of the furnace through a re-sealable fitting and the cover of the furnace closed. The crucible must be located in a uniform temperature region (at least 35 cm from the top) in order to achieve and stably maintain the temperature required for the reaction. An alumina tube 70 cm long with an internal diameter of 1.5 mm and an outer diameter of 3 mm is then inserted from the top in the chamber. The tube has been previously coated with boron nitride in order to improve the thermal shock resistance of alumina. The fiberscope camera that monitors the insertion process ensures the alignment between the injection tube and the crucible. Once the alignment is completed, the camera is extracted and the fittings placed. A vacuum pump is then connected to the furnace and the chamber evacuated for 20 minutes. After this, the furnace is flushed with High Purity Argon Grade 5 for 15 minutes. These last two steps have been repeated four times to minimize the oxygen content. At this point, the furnace is turned on. The temperature is measured by two K-type thermocouples: one in the furnace walls and the other inside the crucible. During the heating process an Argon flux of 0.2 l/min has been kept constant in the furnace. Once the melt has reached 1273 K the alumina tube is dipped in the crucible and the nitrogen-bearing gas -  $N_2$  or  $NH_3$  - is injected in the melt with a flow rate of 0.1 l/min and gas pressures of 0.1 MPa. Two high capacity oxygen-and moisture-removal traps have been put in series and the gas bubbled through them before reaching the furnace – Figure 15. Each trap can lower the oxygen content to less than 1 ppb and moisture levels to less than 10 ppb.

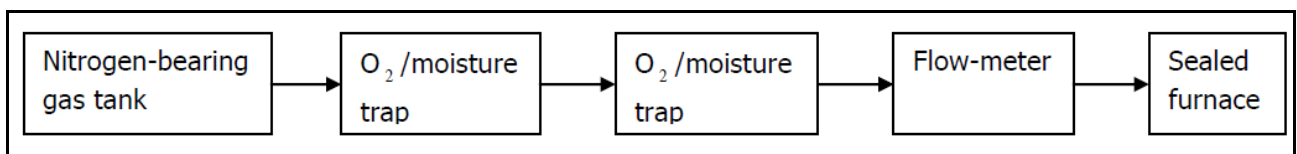


**Figure 15: Apparatus layout**

During the bubbling process, the temperature of the melt has been maintained in the range of 1273-1323 K. Once the gas injection is completed, the tube is extracted from the crucible and the melt let cool down under Argon atmosphere inside the furnace.

### 3.1.2 *Sample preparation and analysis*

#### *Alloy composition*

Mass spectrometry was used to determine the exact alloy composition after casting – specially since Mg easily volatilizes. The samples were first ground with 120  $\mu\text{m}$  SiC paper on a BUEHLER

Metaserv 2000 grinder-polisher and then analyzed with the mass spectrometer - Spectramax from SPECTRO Analytical. Five measurements were made on each sample and the values averaged.

### *Sample preparation*

Samples have been taken from bottom, middle and top part of the crucible so that reinforcement distribution can be characterized.

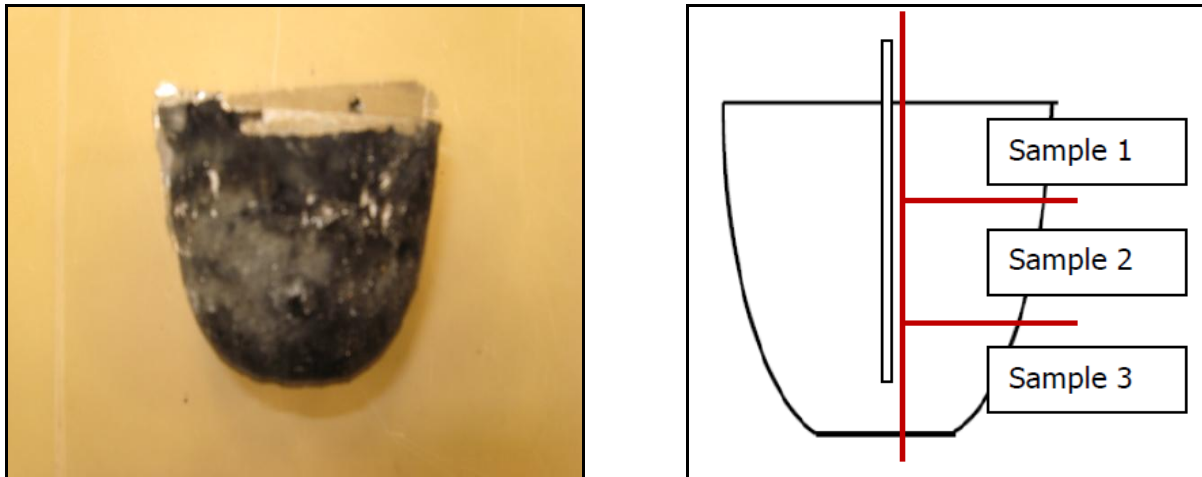


**Figure 1629: a) Picture of sample; b) Methodology of characterization of the casting**

Samples 1 cm thick have been cut for microstructure observation (Scanning Electron Microscope) while for the diffraction pattern analysis (X-ray diffraction) thinner slices 2 mm thick have been attained. The specimens for the microstructure observation were mounted in EXTEC green phenolic powder using an EXTEC MPress mounting machine. The procedure for manual polishing that was followed is given below:

1. Grinding with SiC paper with grit dimensions ranging from 120  $\mu\text{m}$  to 1.2  $\mu\text{m}$ ;
2. Polishing with three cloths using de-agglomerated  $\alpha$ -alumina powder from BUEHLER with dimensions of 1  $\mu\text{m}$ , 0.3  $\mu\text{m}$ , and 0.05  $\mu\text{m}$ . The polishing machine employed is Century E-plus grinder-polisher;
3. Final polishing with velvet cloth using a colloidal silica suspension from BUEHLER to attain a mirror surface;
4. Cleaning with ultrasonic cleaner machine from BUEHLER to remove residuals of alumina and colloidal silica that tends to stick on the sample surface.
5. Sputter-coating with carbon to make the AlN particles conductive for the SEM characterization.

### Sample analysis

XRD analysis has been performed in order to detect the presence of nitrides and secondary phases. Field Emission Gun SEM has been employed for microstructure observation, EDS analysis and X-ray mapping.

#### 3.1.3 Matrix of experiments

<i>Experiment number</i>	<i>Matrix composition</i>	<i>Nitrogen-bearing gas</i>	<i>Gas injection time</i>
1	Pure Al	N <sub>2</sub>	30 min, 1 h, 2 h
		NH <sub>3</sub>	
2	Pure Al + 15% Mg <sup>1</sup>	N <sub>2</sub>	30 min, 1 h, 2 h
		NH <sub>3</sub>	
3	Pure Al + 15% Mg + 8% Si	N <sub>2</sub>	30 min, 1 h, 2 h
		NH <sub>3</sub>	

**Table 4: Matrix of experiments**

## 3.2 Results and Discussion

In order to interpret the reliability of the model, it is first necessary to present the results of the microstructure analysis of the experiments.

### 3.2.1 Microstructure analysis

Experiments 1 and 2 were conducted in a non-inert atmosphere to clarify the role of oxygen content on process feasibility. No nitrides have been detected. If the chamber is not evacuated and flushed with Argon, the large amount of oxygen contained in the atmosphere completely hinders the nitridation reaction and alumina oxides ( $Al_2O_3$ ) form on the top of the casting. Oxidation reaction is indeed more favorable than nitridation since it requires a lower Gibbs energy of formation –see Paragraph 1, Figure 2a-. It is therefore necessary to carry out the gas-liquid

process under an *evacuated and inert atmosphere*. This justifies the failure of previous experiments where an open induction furnace was used.

### *Set of experiments 1*

Pure Al has been bubbled with both nitrogen and ammonia gas for 30 minutes, 1 hour and 2 hours under evacuated and inert atmosphere. XRD analysis of the top (sample 1), the middle (sample 2) and the bottom (sample 3) of the crucible revealed that no nitrides were formed in the casting. This result suggests that a catalyst –such as Mg- needs to be added to the metal in order for the nitridation reaction to occur. This has been also noticed from previous works –see Paragraph 1.

### *Set of experiments 2*

In order to investigate the role of magnesium on the nitridation reaction, 15% wt. has been added to pure Al (experiment 2). Different results have been attained depending on the bubbling time. When the de-oxidized nitrogen is injected in the melt for 30 minutes no aluminum nitrides are detected in the casting. A layer of magnesium nitrides has been noticed on the top of the casting and attached to the walls of the furnace chamber. The powder can be easily recognized for its typical yellowish color –Figure 17.



**Figure 17: Yellowish layer of magnesium nitrides on the surface of the casting**

Zheng et al. [8], Pech-Canul et al. [10], Hou et al. [2] also observed the formation of  $Mg_3N_2$  in Al-Mg-N systems. From a thermodynamic perspective –Figure 18- nitridation of both Al and Mg is very favorable. AlN has higher thermal stability than magnesium nitride over the entire temperature range.

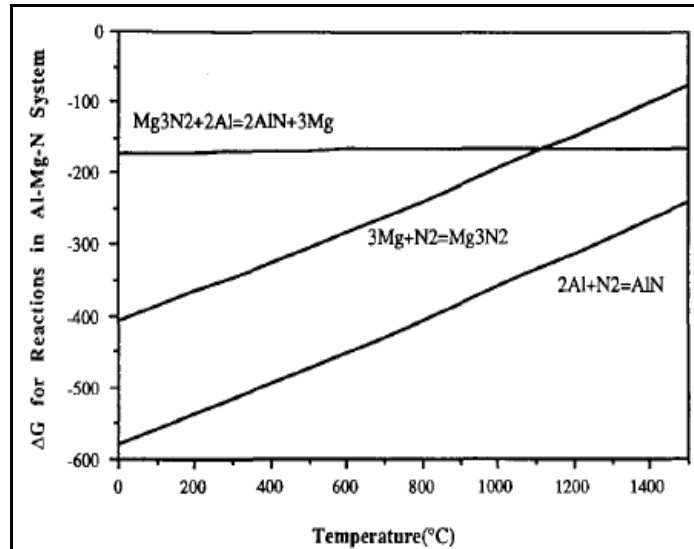


**Figure 18: Ellingham diagram for Al-Mg-N systems [2]**

However, the formation of magnesium nitride is a much more favorable reaction than that of aluminum nitride at around 1273 K in the vapor phase. Since AlN is more stable than  $Mg_3N_2$  at high temperatures, nitrogen first reacts with Mg in the vapor phase –Equation 23- and then molten aluminum reacts with  $Mg_3N_2$  to form AlN through the substitution with Mg –Equation 24-.



Despite this, no AlN have been detected in the casting. This suggests that there must be a step between reaction 23 and 24 that hasn't been underlined by previous investigations and that hasn't occurred in our case. AlN might not form by substitution with Mg (*indirect nitridation*) but some other factors might be involved in the reaction.

The nitrogen gas has then been injected in the Al-Mg melt for 1 h, and in this case a consistent amount of nitrides has been observed. XRD analysis confirms strong peaks of AlN in the upper part of the crucible only (sample 1) along with MgO (periclase) – Figure 19. SEM analysis confirms the presence of AlN with two different morphologies: embedded in the microstructure –Figure 20- or as AlN + MgO powder. Such powder creates pockets distributed in the upper portion of the crucible – Figure 21 and 22.

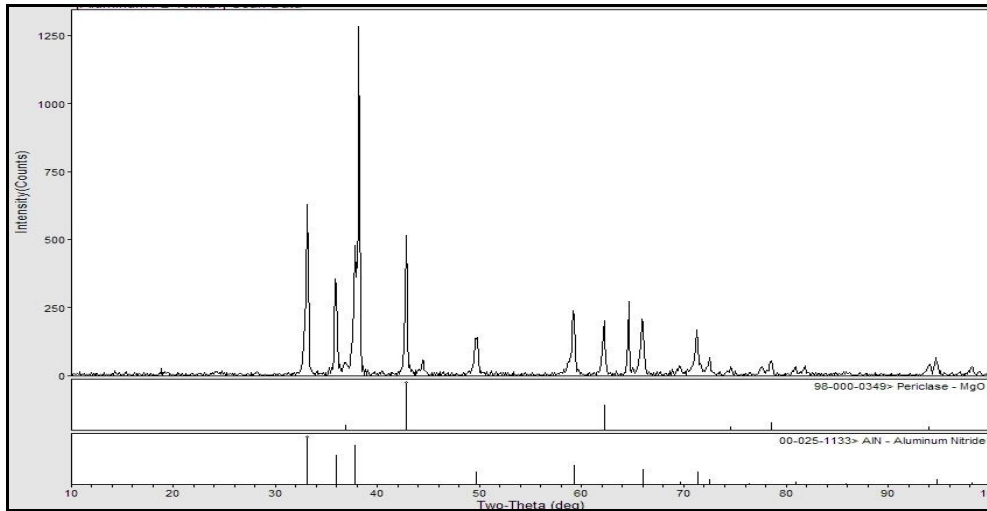


**Figure 19: XRD pattern of the upper part of the crucible for 1 h injection time. Set of Experiments 2.**

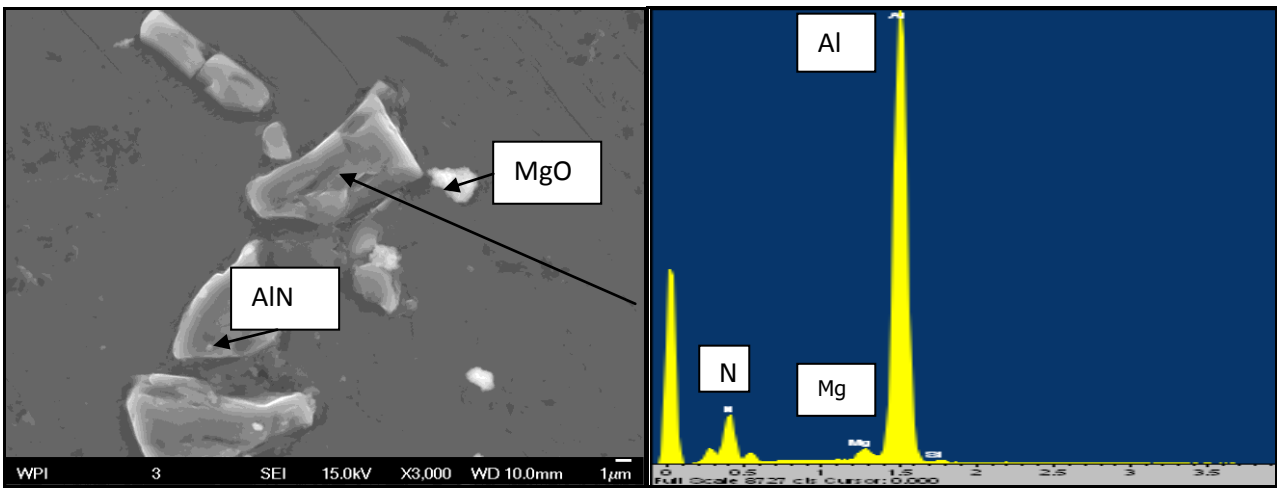


**Figure 30: a) SEM image of AIN imbedded in the matrix in the upper part of the crucible; b) EDS analysis.**

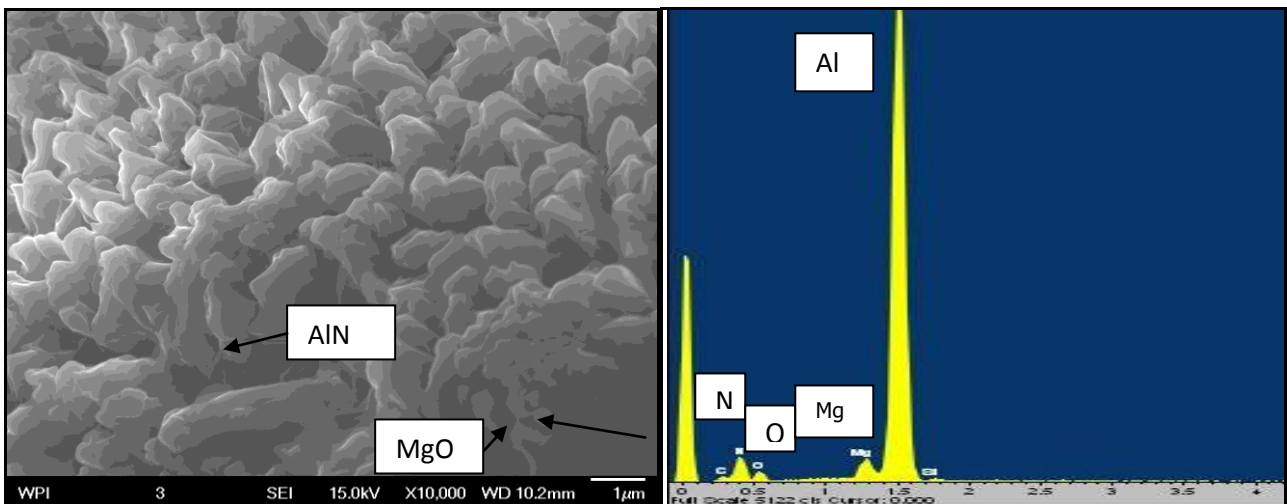


**Figure 31: a) Pockets of AIN and MgO powder in the upper part of the crucible; b) EDS analysis**

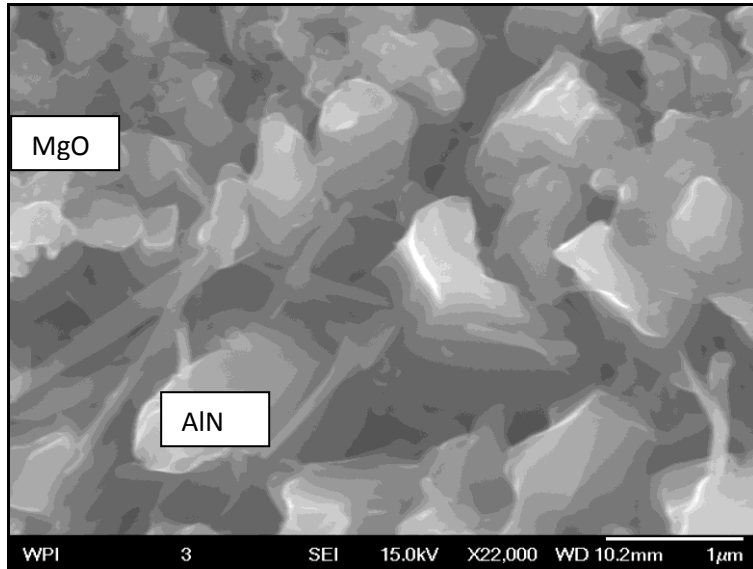


**Figure 22: AlN and MgO phase in the upper part of the crucible at higher magnification**

In the powder phase, MgO is located on the AlN particles and tightly connected with them. The size of the aluminum nitrides ranges from 1 to 3  $\mu\text{m}$  while submicron MgO has been detected. On the other side, no  $\text{Mg}_3\text{N}_2$  has been found in the casting or on the furnace walls. The connection between MgO and AlN and the total absence of  $\text{Mg}_3\text{N}_2$  suggests a different theory on the formation of aluminum nitrides. Once the magnesium nitrides are formed, the phase falls in the melt at lower temperatures (possibly during cooling) and capture  $\text{O}_2$ , synthesizing the MgO phase. The oxygen content in the melt is therefore further reduced and AlN forms by direct nitridation reaction. In this case, the nitridation reaction wouldn't be *indirect* by substitution with Mg but a *direct Mg-assisted* reaction. The Ellingham diagram –Figure 23- shows the thermodynamic stability of MgO over a wide range of temperatures.

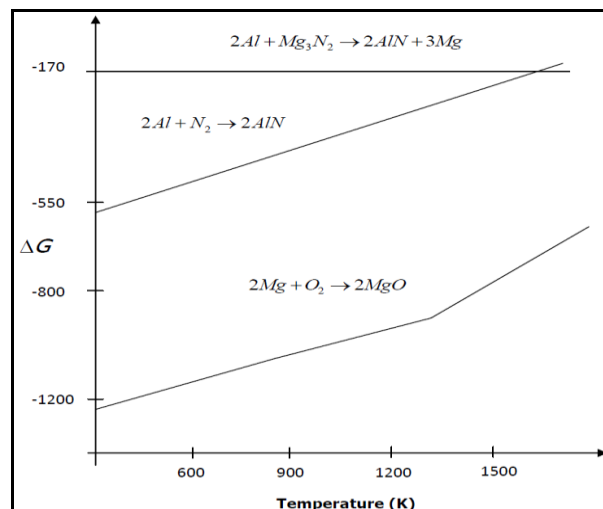


**Figure 23: Ellingham diagram for MgO, AlN and Al-Mg substitution reaction [19]**

The bubbling time has been further increased to 2 hours. In this case, AlN has been observed in the whole microstructure. They are always present in two different morphologies (embedded in the microstructure –Figure 25- and pockets of powder –Figure 26) but XRD analysis reveals AlN and MgO peaks also in the middle/bottom part of the crucible. The peaks in this last location are less intense than at the top of the crucible –Figure 24-, where instead the XRD patterns coincide with the one of Figure 19. This means that the AlN amount is smaller compared to the upper part of the crucible. It can be noticed by naked eye that the distribution of the pockets of powder in this case corresponds to the distribution profile simulated by the 2D model –see paragraph 3-, while in the previous experiment they were situated only at the top of the casting –Figure 27-.

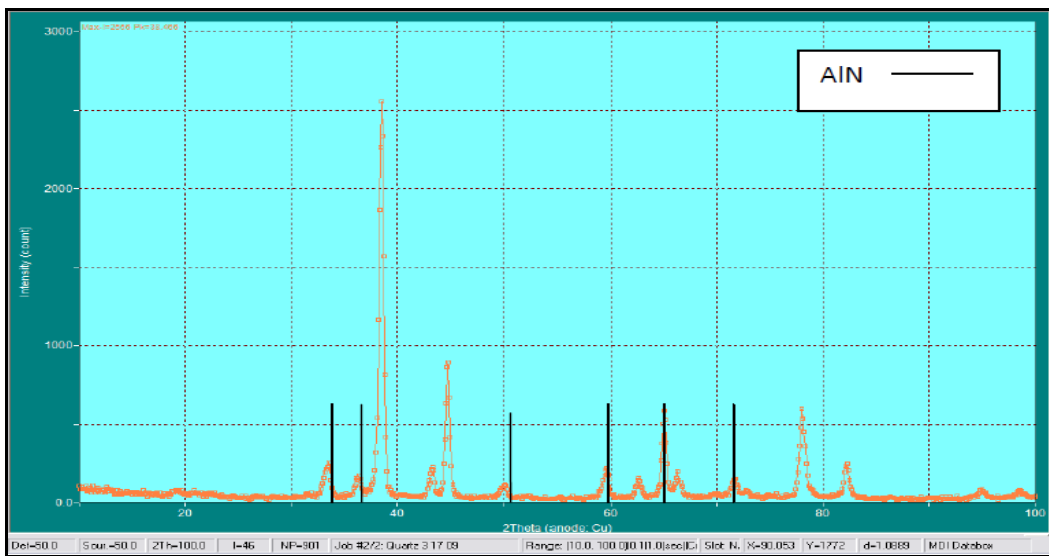


**Figure 24: XRD pattern of the middle part of the crucible**

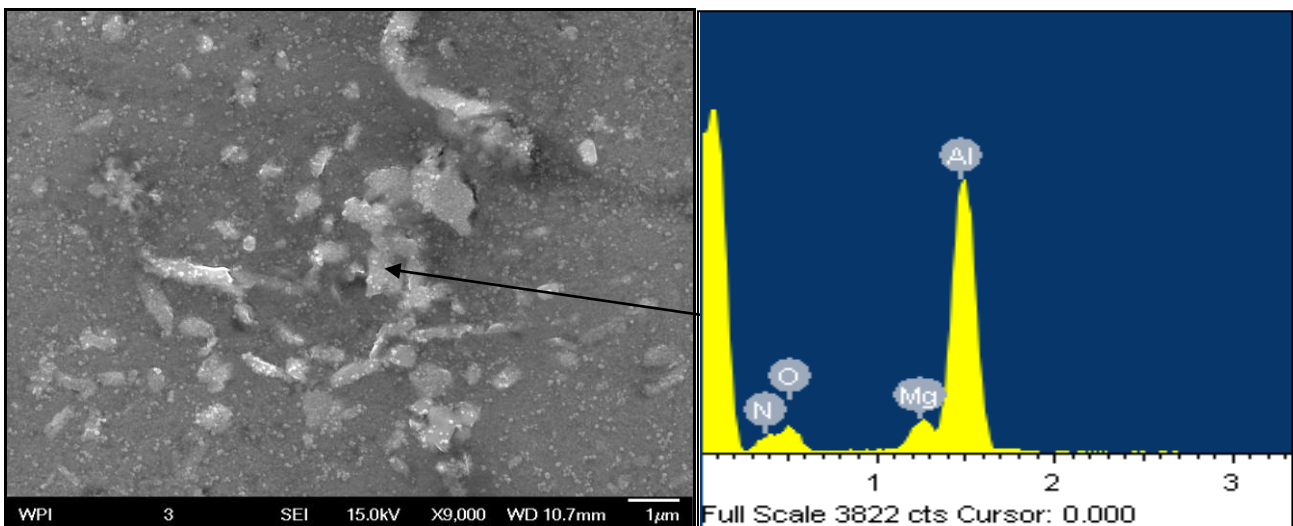


**Figure 325: a) SEM image of AlN imbedded in the matrix in the middle part of the crucible; b) EDS analysis.**

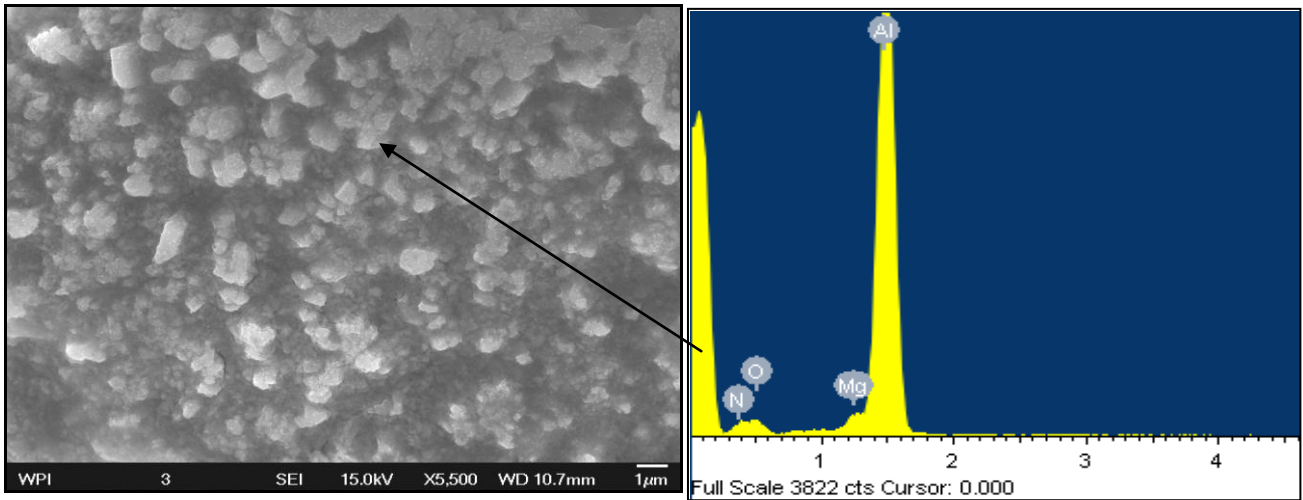


**Figure 26: a) Pockets of AlN and MgO powder in the middle part of the crucible; b) EDS analysis.**

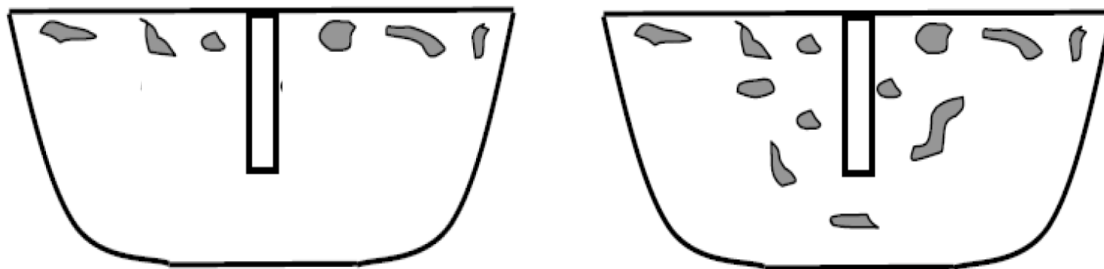


**Figure 27: a) Reinforcement distribution for bubbling time 1 hour; b) for 2 hours.**

It can be noticed that the average size of AlN is smaller compared to shorter bubbling times. It is around 1 μm for the particles embedded in the microstructure and around 0.5 μm in the powder phase. Size control still remains an issue that will be object of further investigation –see Paragraph 4.

No difference has been noticed in AlN formation between the use of ammonia and nitrogen gas. Ammonia quickly dissociates into nitrogen and hydrogen when it's still in the injection tube. Despite this, the use of ammonia is undesirable because of the high amount of porosity that has been observed for long injection times -2 hours-. The phenomenon could be explained in the following way. The fraction of AlN formed is initially limited to the upper portion of the melt which increases the viscosity of the melt in this region. As a result, the melt traps more hydrogen and porosity arises –Figure 28.

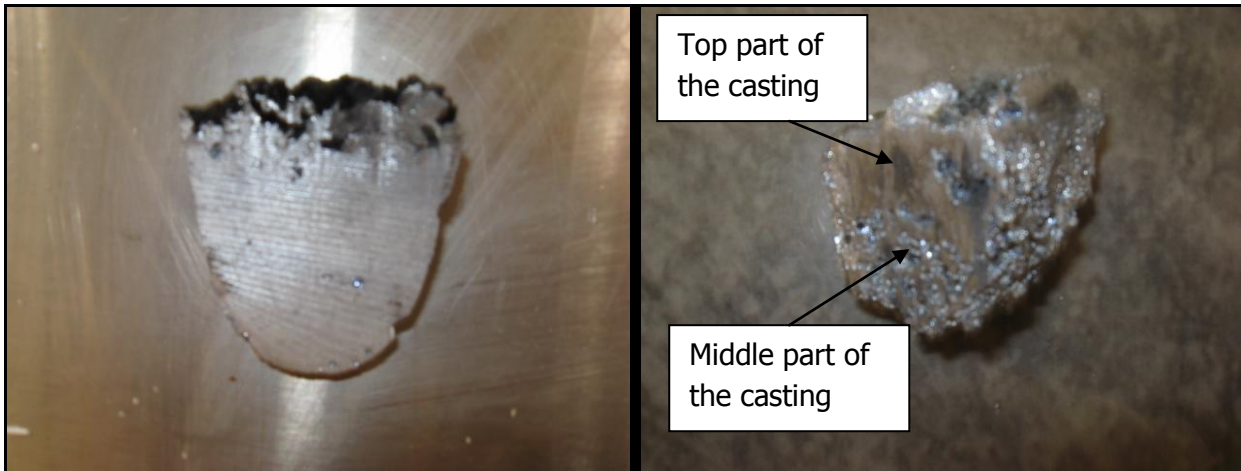


**Figure 28: a) Al-Mg sample processed with nitrogen for 2 hours. Very little porosity detected; b) Al-Mg sample processed with ammonia for 2 hours. Severe porosity can be seen in the middle part of the casting.**

### *Set of experiments 3*

Silicon is a very important element for fluidity and its influence on the nitridation of aluminum needs to be investigated. The literature gives contradictive information about its effect when it's added to the melt together with magnesium. In set of experiments 3 the 8% wt. of Si has been added to the melt together with magnesium. In set of experiments 3 the 8% wt. of Si has been added to the Al-Mg melt. No aluminum nitrides have been detected in the casting both for nitrogen and ammonia. Even when the gas is injected for 2 hours, AlN hasn't been detected in the microstructure. XRD pattern reveals strong peaks for the silicide phase ( $Mg_2Si$ ) –Figure 29-

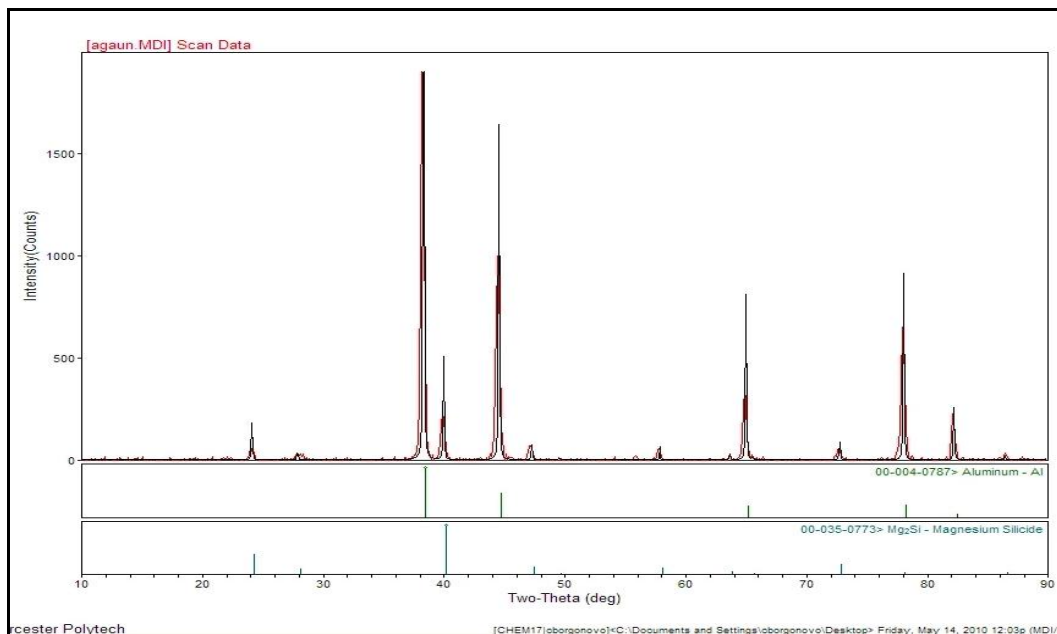


**Figure 29: XRD pattern of Al-Mg-Si microstructure- Set of experiments 3.**

EDS and X-ray mapping confirms the massive presence of the magnesium silicide precipitate – Figure 31 and 32-. The lack of MgO in the microstructure suggests that the synthesis of  $Mg_2Si$  is favorable compared to MgO; the Mg in the melt is depleted by the precipitation of the silicides. In this case, an important observation concerning the temperature of formation of MgO –and therefore of AlN- can be drawn. The formation of magnesium silicide starts at 680 C° and is completed at 550 C° -Figure 33-. Consequently, MgO formation must occur at temperatures equal or smaller than these. This would indicate that the nitridation of aluminum takes place not at temperatures around 1273 K but during the cooling process.

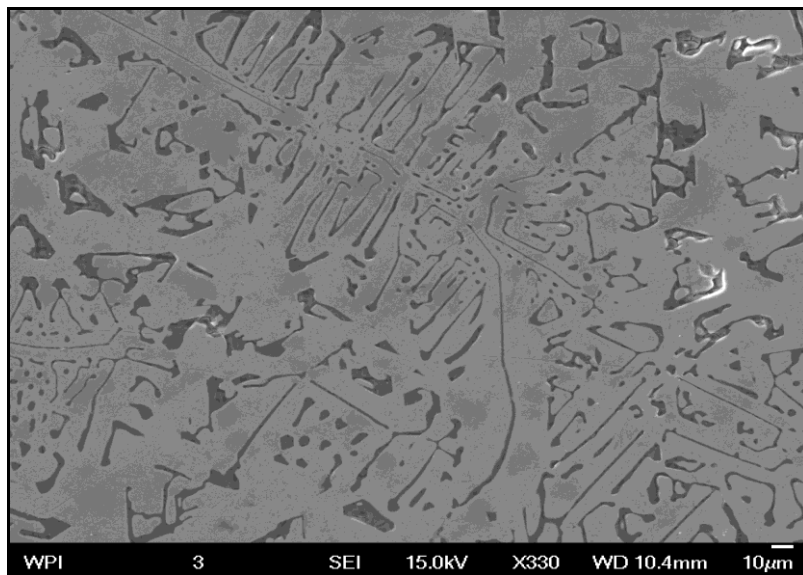


**Figure 330: SEM image of the magnesium silicide phase**

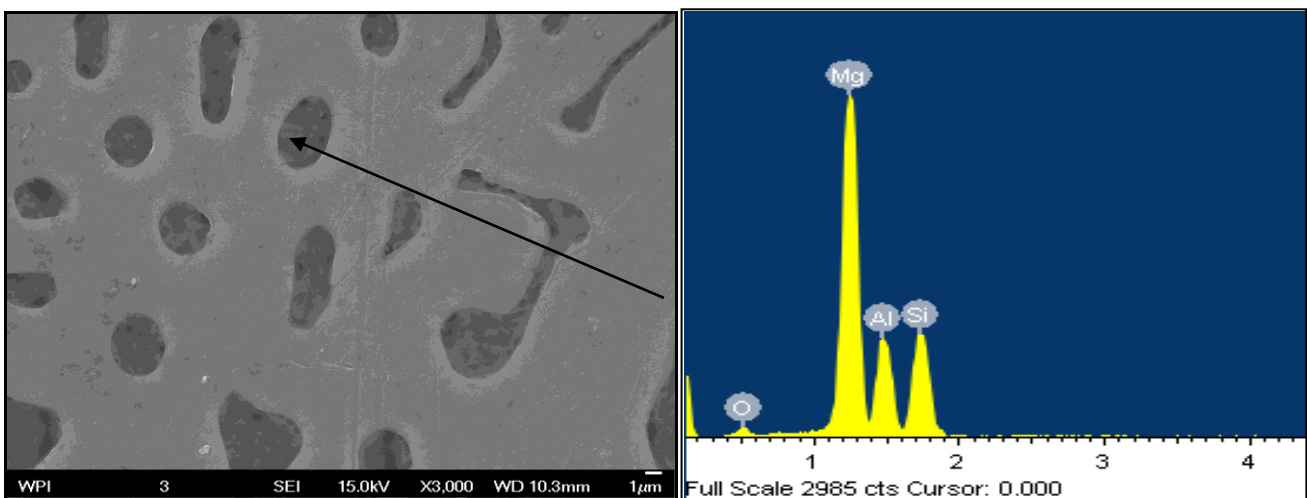


**Figure 31: a) SEM magnification of the magnesium silicide phase; b) EDS analysis**

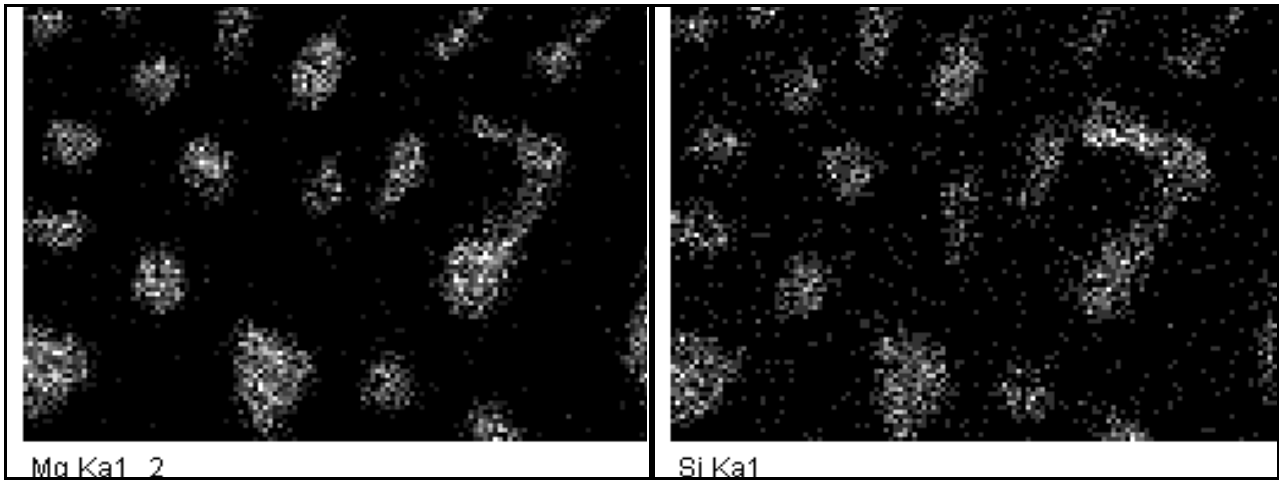


**Figure 32: a) X-ray mapping of magnesium silicide: Mg; b) Si**

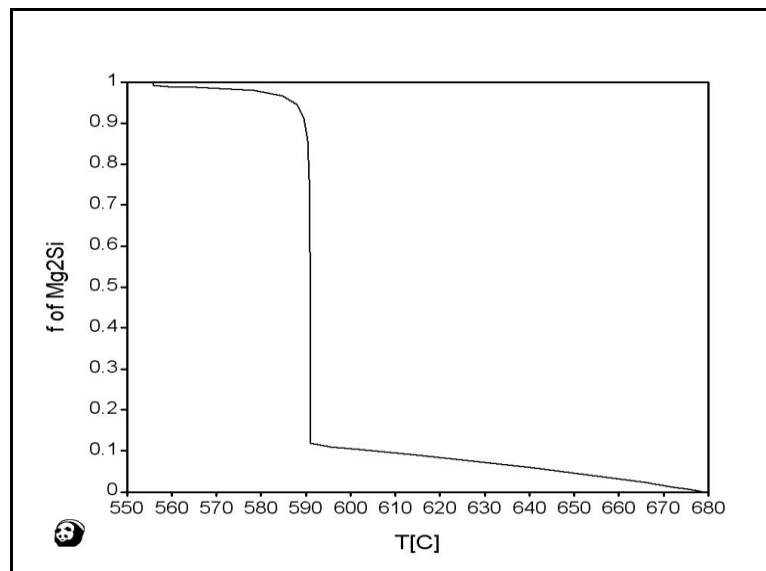


**Figure 33: Fraction solid of magnesium silicide formed vs. temperature (Pandat Software)**

### 3.2.2 Model verification

To confirm the results of the model, the sample have been weighed and compared with the base alloy. The weight loss due to evaporation –Mg easily volatilizes- has been taken into account by pursuing experiments under the same casting conditions but without injecting the gas in the matrix. The difference in molecular weight has been also considered. Table 5 shows the results for the two bubbling times employed when 15% of magnesium is employed. The model has shown good reliability. It can be noticed that it predicts slightly more accurately the weight gain when the gas is injected for a longer time.

<i>Experiment</i>	<i>AlN (g) predicted by the model</i>	<i>AlN (g) detected</i>
Al-Mg bubbled for 30 minutes	2.05	0
Al-Mg bubbled for 1 hour	6.78	9.86
Al-Mg bubbled for 2 hours	13.33	11.31

**Table 5: Comparison between experimental and model results**

Despite these results, the model is not robust yet. Indeed, it gives similar values when no Mg is employed in the casting, while the experiments revealed the total absence of AlN in the casting. The same applies for the series of experiments 3. It is necessary to take into account two factors: the role of catalysts on the nitridation reaction –Mg enhances AlN formation while Si hinders it– and the influence of impurities such as oxygen.

#### 4. Conclusions

- The gas-assisted nitridation reaction of aluminum **has been proved to be feasible**. AlN particles, whose thermal and electrical properties are exceptional, have been successfully synthesized.
- The experimental results show **good agreement** with the model. Despite this, the model needs to be improved by taking into account the role of alloying elements and the detrimental effect of oxygen on the nitridation reaction.
- Particle sizes in the **sub-micron range** have been achieved when the gas is bubbled for 2 hours.
- The distribution **is improved for longer injection times**. For shorter bubbling times -1 hours- the AlN have been traced only on the upper part of the crucible, while for longer times -2 hours- they are located also in the middle/bottom part.
- Ammonia doesn't improve the rate of formation of the reaction and causes an **increase in porosity** for longer bubbling times. This could be due to the entrapment of hydrogen from the upper part of the crucible where the viscosity is higher because of the AlN and MgO formed at an early stage.
- **Oxygen content must be minimized**. The evacuation and flushing of the furnace chamber with Argon to reduce the oxygen amount is necessary for the process to be

feasible. In fact, no nitrides have been detected when the experiments were carried out in a non-inert atmosphere.

- The addition of Mg in the casting is fundamental for the mechanism of formation of AlN. When pure aluminum was used as matrix, no reinforcement was formed. XRD analysis and SEM observation showed the presence of MgO along with AlN. This suggested an alternative hypothesis about the mechanism of formation of nitrides. Magnesium nitrides fall in the melt and Mg bonds with oxygen to create MgO. The oxygen content is lowered and AlN form through direct nitridation or better, a ***direct Mg-assisted nitridation***.
- **Silicon totally hinders the nitridation reaction.** Magnesium silicide and no MgO have been detected. This suggests that the formation of MgO is suppressed by  $Mg_2Si$ . Since the latter precipitates during cooling from high temperatures, aluminum nitridation might also take place at *lower temperatures during cooling*.

### *List of symbols*

$W_{AlN}$  : total amount of AlN formed (mol);

$t$  : bubble residence time (s);

$A_i$  : total gas-liquid interface (m<sup>2</sup>);

$\theta_{AlN}$  : rate of formation of AlN (mol/s m<sup>2</sup>) ;

$d_b$  : bubble diameter (m);

$N_b$  : number of gas bubbles in the melt;

$A_i$  : area of a gas bubble (m<sup>2</sup>);

$E$  : enhancement factor;

$K_L$  : mass transfer coefficient (m/s);

$C^*$  : nitrogen concentration at the gas-liquid interface (mol/m<sup>3</sup>);

$C_i$  : initial nitrogen concentration in the melt (mol/ m<sup>3</sup>);

$P_G$  : pressure of the gas bubble (Pa);

$He$  : Henry's constant (Pa m<sup>3</sup>/mol);

$R$  : ideal gas constant (m<sup>3</sup>Pa/K mol);

$T$ : temperature (K);

$D$ : diffusion coefficient of nitrogen in aluminum ( $\text{m}^2/\text{s}$ );

$P_{GO}$ : initial condition for the pressure in the gas bubble (Pa);

$\gamma$ : gas-liquid surface energy (Pa m);

$P_l$ : hydrostatic pressure in the liquid (Pa);

$\rho_{l,g}$ : liquid and gas density ( $\text{kg}/\text{m}^3$ );

$h$ : crucible depth (m);

$g$ : gravity acceleration ( $\text{m}/\text{s}^2$ );

$P_{atm}$ : atmospheric pressure (Pa);

$d_{no}$ : nozzle diameter (m);

$\tau$ : bubble residence time in the melt (s);

$f_b$ : frequency of bubble formation (1/s);

$V_g$ : the volume flux of the gas at the nozzle ( $\text{m}^3/\text{s}$ );

$V_{bo}$ : volume of the detaching bubble ( $\text{m}^3$ );

$d_{bo}$ : diameter of the detaching bubble (m);

$U_b$ : instantaneous bubble rising velocity (m/s);

$P_{in}, T_{in}, V_{in}$ : state of the gas at the inlet of the tube (Pa, K,  $\text{m}^3/\text{s}$ );

$t_d$ : local diffusion time for Higbie's theory (s);

$\delta$ : liquid boundary layer for Higbie's theory (m);

$k_c$ : kinetic constant of the nitridation reaction ( $\text{m}^3/\text{mol s}$ );

$D_{Al}$ : diffusion coefficient of Al ( $\text{m}^2/\text{s}$ );

$C_{Al}^*$ : aluminum concentration at the bubble surface ( $\text{mol}/\text{m}^3$ );

$\eta$ : aluminum dynamic viscosity (Pa s);

MWN: molecular weight of nitrogen (Kg/mol);

MWA: molecular weight of aluminum (Kg/mol);

$h_{no}$  : nozzle depth (m);

$Q$ : gas flow rate (l/min);

$t_b$  : bubbling time (s);

$\nu$  : kinematic viscosity of the liquid (Pa s m<sup>3</sup>/kg).

## References

1. S.C. Tjong, Z.Y. Ma: "Microstructural and mechanical characteristics of in situ metal matrix composites", *Materials Science and Engineering*, 29, 200, pp. 49-113.
2. Q. Hou a, R. Mutharasan, M. Koczak: "Feasibility of aluminium nitride formation in aluminum alloys", *Materials Science and Engineering A195*, 1995, pp. 121-129.
3. S.Tyagi, Q.Zheng and R. Reddy: "In-situ synthesis of AlN reinforced Magnesium Alloy Composites Using Gas Bubbling method", *Aluminum 2004*, TMS.
4. H.Z. Ye, X.Y. Liu, B. Luan: "In situ synthesis of AlN in Mg–Al alloys by liquid nitridation", *Journal of Materials Processing Technology*, 166, 2005, pp. 79–85.
5. J. Haibo, K. Chen, Z. Heping, S. Agathopoulos, O. Fabrichnaya, J.M.F. Ferreira : "Direct nitridation of molten Al(Mg,Si) alloy to AlN", *Journal of Crystal Growth* 281, 2005, pp. 639–645.
6. Zheng and Reddy, "Kinetics of In-Situ Formation of AlN in Al Alloy Melts by Bubbling Ammonia Gas", *Metallurgical and Material Transaction* 34B, 2003, pp. 793-805.
7. Zheng, Wu, Reddy, "In-Situ Processing of Al Alloy Composites", *Advanced Engineering Materials* 5, No. 3, 2003, pp. 167-173, 2003
8. Zheng, Reddy, "Mechanism of in-situ formation of AlN" in Al melt using nitrogen gas", *Journal of Material Science* 39, 2004, pp. 141-149.
9. P. Shtapitanonda and J. Magrave: "Kinetics of nitridation of Mg and Al", *Symposium at University of Wisconsin-Madison*, 1956.
10. M. I. Pech-Canul, R.N. Katz and M. M. Makhlof, "Optimal Parameter for Wetting SiC by Aluminum Alloys", *Metallurgical and Materials Transactions* 31A, 2000, pp. 565-573.
11. Scholz and Greil, "Nitridation reactions of molten Al-(Mg, Si) alloys", *Journal of Material Science*, 26, 3, 1991, pp. 669-677.
12. L. Jinxiang , Gao Xiuying , C. Jianfeng , W. Qun, S. Yuhui, G. Qin: "Study of the kinetics of the nitridation reaction on Al-(Mg,Si) alloys by TG", *Thermochimica Acta*, 253, 1995, pp. 265-273.
13. J. Szekely, "Fluid flow phenomena in metals processing", *Academic Press* 1979.
14. Tsuge, Terasaka, Koshida, Matsue, "Bubble formation at submerged nozzles for small gas flow rate under low gravity", *Chemical Engineering Science*, 52, 1997, pp.3415-3420.

15. Takemura, Matsumoto, "Dissolution of spherical carbon dioxide bubbles in strong alkaline solutions", Chemical Engineering Science 55, pp. 3907-3917.
16. Madhavi, Golder, Samanta, Ray, "Studies on bubble dynamics with mass transfer", Chemical Engineering Journal 128, 2007, pp. 95-104.
17. M. J. Assael and K. Kakosimos: "Reference Data for the Density and Viscosity of Liquid Aluminum and Liquid Iron", J. Phys. Chem. Ref. Data, 35, 1, 2006.
18. R.A. SaravananI, J.M. Molina, J. Narciso, "Effects of nitrogen on the surface tension of pure aluminium at high temperatures", Scripta mater. 44, 2001, pp. 965–970.
19. Ellingham diagram tutorial: <http://www.engr.sjsu.edu/ellingham/tutorial.html>.

### *Table of Figures*

Figure 1: Schematic of in-situ gas/liquid process .....	46
Figure 2: a) : Ellingham diagram for the nitridation and oxidation of aluminum [19]; b) Oxygen partial pressure for nitridation vs. temperature.....	47
Figure 3: Z-axis and x-axis distribution .....	49
Figure 4: Schematic of the diffusion domain in the liquid (Higbie's penetration theory) .....	53
Figure 5: Domain for the calculation of the bubble diamete .....	54
Figure 6: Domain for the calculation of the distribution of the gas bubbles in the crucible .....	54
Figure 7: Mesh of the 1D domain .....	55
Figure 8: Mesh of the 2D domain .....	55
Figure 9: Global Equations Mode.....	56
Figure 10: Boundary Integration Variables Mode.....	56
Figure 11: 2D domain boundary conditions .....	57
Figure 12: Sub-domain settings of the Bubbly Flow Module.....	58
Figure 13: Bubble radius vs. distance from the bottom if the crucible .....	60
Figure 14: Experimental set-up.....	18
Figure 15: Apparatus lay-out.....	20
Figure 16: a) Picture of sample; b) Methodology of characterization of the casting.....	63
Figure 17: Yellowish layer of magnesium nitrides on the surface of the casting.....	<b>Errore. Il segnalibro non è definito.</b>
Figure 18: Ellingham diagram for Al-Mg-N systems [2].....	66

Figure 19: XRD pattern of the upper part of the crucible for 1 h injection time. Set of Experiments 2. ....	67
Figure 20: a) SEM image of AlN imbedded in the matrix in the upper part of the crucible; b) EDS analysis. ....	67
Figure 21: a) Pockets of AlN and MgO powder in the upper part of the crucible; b) EDS analysis. ....	67
Figure 22: AlN and MgO phase in the upper part of the crucible at higher magnification .....	68
Figure 23: Ellingham diagram for MgO, AlN and Al-Mg substitution reaction [19] .....	68
Figure 24: XRD pattern of the middle part of the crucible.....	69
Figure 25: a) SEM image of AlN imbedded in the matrix in the middle part of the crucible; b) EDS analysis. ....	69
Figure 26: a)Pockets of AlN and MgO powder in the middle part of the crucible; b) EDS analysis. ....	70
Figure 27: a) Reinforcement distribution for bubbling time 1 hour; b) for 2 hours. ....	70
Figure 28: a) Al-Mg sample processed with nitrogen for 2 hours. Very little porosity detected; b)Al-Mg sample processed with ammonia for 2 hours. Severe porosity in the middle part of the casting. ....	71
Figure 29: XRD pattern of Al-Mg-Si microstructure- Set of experiments 3. ....	71
Figure 30: SEM image of the magnesium silicide.....	72
Figure 31: a) SEM magnification of the magnesium silicide phase; b) EDS analysis.....	72
Figure 32: a) X-ray mapping of magnesium silicide: Mg; b) Si .....	73
Figure 33: Fraction solid of magnesium silicide formed vs. temperature (Pandat Software) .....	73

## Recommendations for future work

Feasibility of the in-situ gas-liquid process has been proved. The investigation will move forward and the experimental aspect will be privileged. The following points will be improved:

- *Experimental apparatus:* the apparatus employed in the experiments –see Appendix C- was not optimal. Oxygen leaks in the furnace used to occur even after evacuation and Argon flush have been carried out. Moreover, the maximum temperature in the furnace was limited to 1273 K in the bottom part. A more compact and precise apparatus needs to be designed and build in order to pursue a correct analysis of the mechanism according to which aluminum nitridation occurs and tailor matrix composition. Moreover, the current apparatus required extremely long process times –up to 2 hours- in order to correctly center the tube in the crucible. A rotating tube could be employed instead of the normal alumina tube in order to stir the metal and break the pockets of powder that have been observed. More than one injection tube or more than one inlet nozzle could also be used.
- *Control of particle size and distribution:* a reinforcement size around 1  $\mu\text{m}$  or smaller has been achieved and the distribution improved for longer bubbling times. Despite this, the factors that influence the size of the particles and their distribution in the crucible is not clear yet. In order to scale the particle dimension down to the nano-level, these factors need to be highlighted and analyzed. The distribution of the reinforcement could be improved by causing convection currents in the melt.
- *Effect of alloying elements:* the effect of Mg and Si on the nitridation reaction has been discussed. Despite this, the role of Mg must be further clarified. The effect of other common alloying elements such as Cu and Mn will be also investigated.
- *Synthesis of other types of reinforcements:* the use of other gases, such as borane, will be considered. Borides are very stable and provide excellent mechanical properties.
- *Scalability:* once process optimization will be achieved, the possibility to make it feasible on industrial levels will be studied. Larger matrix quantities will be processed and this will affect the dynamics of the nitridation reaction. In case extremely long process times would be needed to form the nitrides, alternative experimental conditions will have to be formulated.